Quaternary Science Reviews 312 (2023) 108164

Contents lists available at ScienceDirect

Quaternary Science Reviews

journal homepage: www.elsevier.com/locate/quascirev

Drilling 1100-km-long seafloor ridges reveals how palaeoshorelines control carbonate shelf morphologies (North West Shelf, Australia)

Ulysse Lebrec [a, b, *], Rosine Riera [b], Michael O'Leary [a], Jody M. Webster [c], Yusuke Yokoyama [d], Luke A. Gliganic [e], Simon C. Lang [a], Victorien Paumard [a, f]

[a] Centre for Energy and Climate Geoscience, School of Earth Sciences, The University of Western Australia, Crawley, WA, 6009, Australia
[b] Norwegian Geotechnical Institute, Perth, WA, 6000, Australia
[c] Geocoastal Research Group, School of Geosciences, University of Sydney, Sydney, NSW, 2006, Australia
[d] Atmosphere and Ocean Research Institute, The University of Tokyo, 5-1-5 Kashiwanoha, Kashiwa, Chiba, 277-8564, Japan
[e] Centre for Archaeological Science, School of Earth, Atmospheric and Life Sciences, University of Wollongong, Wollongong, NSW, 2500, Australia
[f] UWA Oceans Institute, The University of Western Australia, Crawley, WA, 6009, Australia

ARTICLE INFO

Article history:
Received 3 March 2023
Received in revised form
24 May 2023
Accepted 29 May 2023
Available online xxx

Handling Editor: I Hendy

Keywords:
Paleoshorelines
Paleogeography
Sedimentology-marine cores
Continental shelf
North West Shelf
Carbonate
Pleistocene
Beach ridges
Diagenesis

ABSTRACT

The Rowley Shelf, the southern half of the tropical, carbonate-dominated, North West Shelf of Australia, is covered with linear ridges that can be tracked parallel to the coast over 1100 km between the modern coast and the 140 m isobath. Here, we investigate the origin and nature of these ridges based on the integration of extensive borehole data, high-resolution geophysical data, age dating and compaction analysis.

Our investigation reveals that each ridge consists of now-submerged relict coastal deposits that were formed over the last 200,000 years through wave, tidal, fluvial and aeolian processes. These features were dominantly preserved through early diagenesis and illustrate the longest continuous submerged palaeoshorelines reported to date.

The distribution of relict coastal features, and therefore early diagenesis, controls the morphology of the continental shelf. First, relict coastal features tend to be stacked on top of each other, resulting in the formation of composite diachronous coastal deposits that form distinctive steps on the seabed, up to 10s m high. Second, relict coastal features form a hard substrate that controls the location of coral reefs along the shelf. Reefs, including a 20-m-thick MIS 3 drowned coral reef described here for the first time, as well as modern reefs of the Muiron Islands, Montebello Islands and Dampier Archipelago, are all developed on top of relict coastal features.

The distribution, size and mineralogy of relict coastal features highlight climatic changes along the Rowley Shelf. High relative sea levels (RSL) are associated with low carbonate production and up to 50% of terrigenous grains, while low RSL deposits exhibit increased carbonate production and reduced terrigenous grain content. This asymmetry is interpreted to reflect the onset of the monsoon associated with increased fluvial runoffs during interglacial periods.

Lastly, our work shows that compaction analyses are critical for palaeoenvironment and RSL reconstructions. Indeed, the accumulation of 50 m of sediment on a RSL indicator can result in an offset of the measurement by 12.7 m.

1. Introduction

Tropical carbonate-dominated continental shelves thrive between the equator and the 30th parallels (Laugié et al., 2019) and represent 30% of the world's continental shelves (Longhurst et al., 1987). They form unique depositional environments and are renowned biodiversity hotspots, in particular due to the presence of coral reefs (Wilson, 2013). Coral reefs and other bioconstructed reefs have been extensively studied, sometimes overshadowing the importance of other sedimentary features, and leading to the view that reefs dominate tropical-shelf sedimentary systems (Droxler

* Corresponding author. Centre for Energy and Climate Geoscience, School of Earth Sciences, The University of Western Australia, Crawley WA, 6009, Australia.
E-mail addresses: ulysse.lebrec@ngi.no, ulysse.lebrec@uwa.edu.au (U. Lebrec).

https://doi.org/10.1016/j.quascirev.2023.108164

and Jorry, 2013; Longhurst et al., 1987; Riera et al., 2023). In reality, reefs such as the Australian Great Barrier Reef, Belize Barrier Reef, Florida Keys Reef Tract and New Caledonian barrier reefs consist of relatively thin late-Quaternary deposits overlying antecedent sedimentary substrate (Droxler and Jorry, 2013; Montaggioni et al., 2011; Multer et al., 2002; Purkis et al., 2014; Webster and Davies, 2003). Historical classifications do mention that tropical carbonate shelf morphologies can also be controlled by the formation of non-reefal sand shoals (Ahr, 1973, 1998; Bosence, 2005; Burchette and Wright, 1992; James et al., 1983; Purkis and Harris, 2016), however, the nature of these features and the processes controlling their formation and distribution remain largely understudied.

This research bias affects all fields building directly or indirectly on the understanding of carbonate shelf depositional environments. At present, 60% of hydrocarbon producing reservoirs are located in carbonate-dominated environments (Burchette et al., 2012) and the misinterpretation of their formation mechanisms can have dire consequences on field developments and carbon capture and storage projects. Furthermore, recovery of offshore renewable and non-renewable energy resources requires extensive onsite infrastructures for which knowledge of the seabed sediment and rock properties is critical (International Society of Soil Mechanics and Geotechnical Engineering, 2005). For such applications, carbonate sediments are typically regarded as problematic (Beemer et al., 2018) and their improper characterisation led to major challenges, for example where driven piles were observed to free-fall through the sediments (Khorshid, 1990; Senders et al., 2013; Spagnoli and Scheller, 2016). In addition, relict submerged coastal features forming ridge-like morphologies, which are therefore not bioconstructed, have been found to support rich ecosystems that are associated with increased fish diversity (Aston et al., 2022; Currey-Randall et al., 2021), and are colloquially referred to as Key Ecological Features (Australian Institute of Marine Science, 2022). Similar to bioconstructed reefs, relict coastal features represent key archives of palaeoenvironments and associated relative sea levels (RSLs, Lebrec et al., 2022b; Mauz et al., 2013, 2015). However, they can only be used as such when the sedimentological and hydrodynamic processes affecting the shelf are well understood. Lastly, recent developments in underwater archaeology have built on the reconstruction of submerged landscapes to identify possible early human communities and migration routes (Benjamin et al., 2020; Braje et al., 2019; Wiseman et al., 2021), further demonstrating the need to better understand environmental processes that lead to their formation and subsequent modification.

The North West Shelf (NWS) is a tropical low-angle platform covering an area in excess of 720,000 km^2 dominated (>90%) by carbonate sediments (Jones, 1973; Purcell and Purcell, 1988). It is part of the Western Australian coral-reef province and hosts World Heritage Sites such as Ningaloo Reef, the reef-fringed Montebello Islands and Dampier Archipelago as well as mesophotic reefs (Abdul Wahab et al., 2018; Collins, 2002; Griffith, 2004; Kordi et al., 2016). Recently, the integration of 3D seismic surveys with satellite images and historical datasets increased high-resolution bathymetry coverage by 250,000 km^2 (Lebrec et al., 2021b). This new dataset reveals that some of the most significant bathymetric features of the NWS are relict coastal features formed through wave, tidal, fluvial and aeolian processes, hence suggesting that these non-bioconstructed features have played a key role in the development of the shelf morphology. In fact, these features appear stacked along nine Modal Sea Level Depths (MSLDs) ranging from 20 to 140 m below sea level (bsl) that are continuous over several hundreds of kilometres (Lebrec et al., 2022b).

In order to study the nature of these relict coastal features, we investigated geotechnical cores recovered from four sites throughout the shelf (Fig. 1), intersecting MSLDs 20, 90 and 105. The resulting dataset includes shallow-water cores collected as part of this study, as well as petroleum-development boreholes. These cores provide a unique opportunity to explore the relationship between RSL, the formation and evolution of coastal sedimentary systems and bioconstructed reefs, providing an insight of the key processes driving tropical shelf morphologies.

In this study, we present a detailed lithological description of the sedimentary units, integrated with 2D high-resolution seismic, 3D seismic and high-resolution bathymetry. We also introduce a chronostratigraphic framework of the shelf over the last 200,000 years based on both radiocarbon and optically stimulated luminescence (OSL) measurements. These results are then used to discuss the relationship between climate, coastal processes and RSL, and how they affect the development and architecture of carbonate shelf morphologies.

2. Settings

The NWS of Australia stretches over 2400 km along the tropical northwest margin of Australia (James et al., 2004; Purcell and Purcell, 1988). While the term NWS originally encompassed oil and gas provinces extending to the 2000 m isobath, it is here used to designate the continental shelf alone, in line with Quaternary-geology studies (Baker et al., 2008; James et al., 2004; Lebrec et al., 2022b). The NWS is subdivided into two geographic areas including the Rowley Shelf, the focus of this study (Fig. 1), which extends from Exmouth to the Cape Leveque and, eastward, the Sahul Shelf (Carrigy and Fairbridge, 1954; Wilson, 2013).

The Rowley Shelf is a carbonate-dominated passive margin developed on top of rift-induced basins formed during the breakup of Gondwana and then Pangea (Keep et al., 2007). Present-day accommodation is mainly controlled by subsidence (Cathro and Karner, 2006; Driscoll and Karner, 1998; Romine et al., 1997) and glacio-isostasy (Lambeck and Nakada, 1990; Yokoyama et al., 2001). Locally, tectonic reactivation led to vertical displacements of up to 8 m during the Quaternary (Whitney et al., 2016). The shelf, previously described as a gentle bathymetric ramp, is characterised by regional slope values of less than 1° (James et al., 2004). It is commonly divided in three depth zones that follow fair-weather and storm-weather wave base: the inner shelf [0–50 m], the mid shelf [50–120 m] and the outer shelf [120–200 m] (Dix, 1989; James et al., 2004; Wilson, 2013).

The modern climate is dry through most of the year with rainfall events limited to the summer months when a monsoon-like climate associated with cyclones and tropical depressions prevails (Hesse et al., 2004; Suppiah, 1992). Such events are sufficient to result in the formation of siliciclastic deltas, fed by intermittent rivers (Semeniuk, 1992). The shelf remains however largely dominated by carbonate sediments with siliciclastic deposits restricted to the inner shelf (James et al., 2004). The Rowley Shelf is a coral-reef province and the majority of the shelf islands such as Barrow Island, Montebello Islands, and the Dampier Archipelago, are fringed with corals (Bonesso et al., 2020; Collins, 2002; Griffith, 2004; Moustaka et al., 2019). Locally, mesophotic corals are also documented (Abdul Wahab et al., 2018). Strong water fluxes affect the shelf including the warm, low-salinity Leeuwin current as well as tidal currents, long-period swell and waves in the cross-shelf direction (Baines, 1981; Holloway, 1995, 2001; Katsumata, 2006; Stephen et al., 2009). The combination of these fluxes led to the formation of bedforms throughout the shelf (Belde et al., 2017; James et al., 2004; Lebrec et al., 2022a).

In addition, the seabed is characterised by the presence of numerous palaeoshorelines (Dix et al., 2005; Hengesh et al., 2011; Jones, 1973; Lebrec et al., 2022b). These features were identified

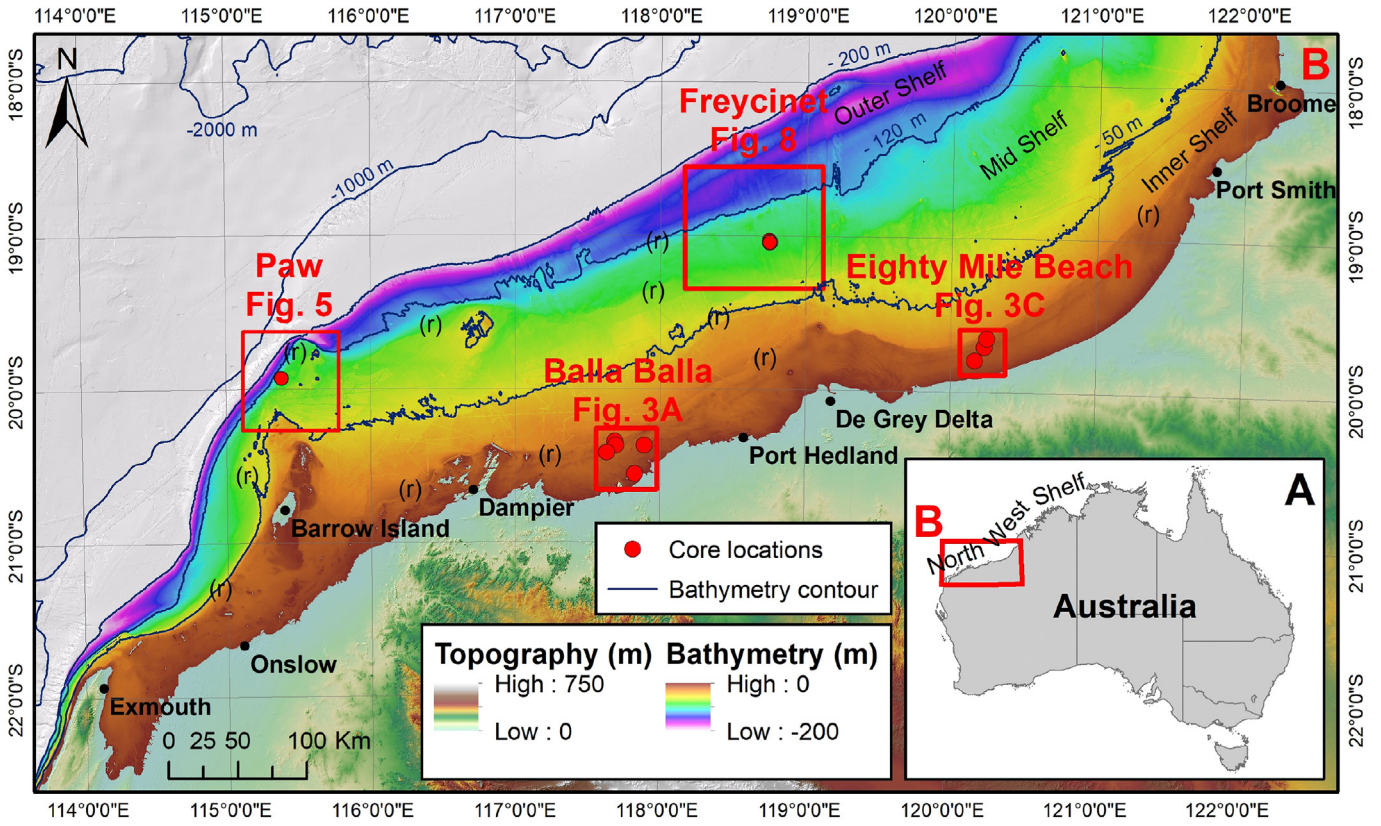

Fig. 1. Location map and coring sites. Background digital elevation models from Lebrec et al., 2021b. Label (r) indicates isobath-parallel linear ridges.

from the shoreline to depths of about 140 m along nine modal sea level depths (MSLDs) and can be tracked continuously along the coast over hundreds of kilometres (Lebrec et al., 2022a, 2022b). Locally, the seabed is riddled with pockmarks resulting from dewatering (Riera et al., 2022), tidal currents (Jones et al., 2009), or fish activity (Mueller, 2015).

Quaternary sedimentation patterns appear to be linked with the evolution of the climate and RSL (Hallenberger et al., 2021). During glacial periods, the monsoon is limited and the climate dryer, resulting in an important production of aragonite (Gallagher et al., 2014, 2018; Hallenberger et al., 2021). In contrast, during interglacial periods, the monsoon is strengthened and the climate wetter (Hesse et al., 2004), leading to increased fluvial runoff and in turn increased siliciclastic sedimentation and reduced aragonite production (Hallenberger et al., 2019). This asymmetry is illustrated by the alternation of ooid-rich, aragonitic strata and calcite-rich bioclastic strata at IODP sites (Hallenberger et al., 2021), but also by the description of kilometre-size ooid-rich embayments along the outer shelf, in opposition with the fluvial-influenced features present along the coast (James et al., 2004; Lebrec et al., 2022b). The discovery of Holocene oolites outcrops near Port Smith and Port Hedland (Hearty et al., 2006; Semeniuk, 1996) and, recently, of modern ooid shoals within the De Grey River delta (Lebrec et al., 2023) indicates that additional studies are required to fully understand Quaternary sedimentary and climatic records along the shelf.

3. Data and methods

3.1. Datasets

This study is based on the integration of high-resolution bathymetry, 2D & 3D seismic and geotechnical datasets. They are summarised in Table 1 and detailed hereafter.

Bathymetry datasets build on the compilation from Lebrec et al. (2021b) including 45,000 km^2 of satellite-derived bathymetry and 132,000 km^2 of seismic-derived bathymetry. This dataset was enriched with bathymetry produced using 3D seismic surveys from TGS. Where possible, regional bathymetry was supplanted with multibeam echosounder data from Geoscience Australia and industry partners. High-resolution 2D seismic datasets contain both regional and site-specific surveys. Regional datasets include seismic lines acquired by Geoscience Australia through multiple cruises between 2005 and 2018. Data quality is variable, and penetration often limited to surficial unconsolidated sediments. Site-specific datasets were provided by industry partners over the Freycinet and Paw areas respectively (Fig. 1). These surveys consist of a mesh of 2D lines spaced by 250–500 m which have a penetration of a few tens of metres.

Geotechnical datasets were acquired during site-specific offshore site investigations. Balla Balla and Eighty Miles Beach cores were collected as part of this study in July 2021 using a subsea drill rig operated by divers. The dataset consists of eight 3 m cores that were drilled in less than 20 m of water depth. The Paw geotechnical dataset was acquired in 2011. Part of this dataset was donated to UWA, including five cores with lengths ranging from 35 to 75 m below mud line (bml). Most cores are discontinuous as multiple intervals were destroyed during geotechnical testing. Freycinet geotechnical dataset was acquired using a portable remotely operated drill. UWA was authorised to access several samples from three boreholes, providing a regular but discontinuous sedimentary record to a depth of 48.5 m, as well as the associated cone penetration tests.

Table 1
Data available.

Data type	Dataset	Data provider	Coverage	Resolution/ Depth	Vertical Accuracy/ retained	Spatial accuracy
Satellite-derived bathymetry	NWS SDB	Lebrec et al. (2021b)	45,000 km^2	10 × 10 m	5%	16 m
Seismic-derived bathymetry	NWS SDB	Lebrec et al. (2021b)	132,000 km^2	30 × 30 m	1%	200 m
Seismic-derived bathymetry	Proprietary seismic surveys including Capreolus	TGS	33,954 km^2	12.5 × 25 m	1%	<1 m
MBES	Paw geophysical surveys	Proprietary	893 km^2	5 × 5 m	1%	<1 m
MBES	Freycinet geophysical surveys	Proprietary	27 km^2	1 × 1 to 3 × 3 m	1%	<1 m
2DHR	Surveys	Geoscience Australia	100 km	Variable	Variable	Variable
2DHR	Paw geophysical surveys	Proprietary	40 km	<1 m	Na	Na
2DHR	Freycinet geophysical surveys	Proprietary	267 km	<1 m	Na	Na
Geotechnical borehole	UWA – TAMS nearshore subsea cores	UWA	8 BHs	3 m	100%	Na
Geotechnical borehole	Paw geotechnical S.I.	Proprietary	5 BHs	Up to 75 m	30%	Na
Geotechnical borehole	Freycinet geotechnical S.I.	Proprietary	3 BHs	Up to 48.5 m	1 sample every 2–3 m	Na

3.2. Data analysis

All datasets were integrated together using GIS databases and IHS Kingdom projects. Due to the lack of site-specific velocity profiles, time-depth relationships used to display geotechnical datasets on top of seismic lines build on nominal velocities of 1700 m/s in unlithified sediments and of 2400 m/s in lithified intervals at Freycinet and of 2100 m/s at Paw, averaged from adjacent petroleum-well sonic velocities (e.g. Willcox-1). Such approach was validated by the good correlation between strong reflectors and major lithology changes.

Cores were described at a macro scale as well as at a micro scale using 140 thin sections, half stained with alizarin red S and potassium ferricyanide. Sediment and rock descriptions were performed following the methodology from IODP expedition 356 which was conducted over the NWS (Gallagher et al., 2017). This approach builds on the texture definition from Dunham and Ham (1962), with modifications from Embry and Klovan (1971) and Stow (2005) that are appended to lithification categories modified from Gealy et al. (1971). Unit names are then associated with a prefix and suffixes representing respectively major (>50%) and minor (<50%) components. For detailed descriptions, a letter is used to indicate the relative percentage of each component: D: dominant (>80%); A: Abundant (50–80%; C: Common (10–50%), F: Few (1–10%), R: Rare (<1%) and T: Trace. Grain sizes and sorting were defined following the classification from Wentworth (1922) and Folk and Ward (1957). Diagenetic features were described following the terminology from Scholle and Ulmer-Scholle (2003). The term microcrystalline cement was however preferred over micrite to avoid confusion between carbonate ooze and cements, in line with comments from James and Jones (2015) and recommendations from Friedman (1985). The mineralogy composition of 40 bulk samples was determined by random-powder X-ray diffraction analysis using a Panalytical Aeris diffractometer. Intensity curves were interpreted using the software High Score Plus and a Retvield fit.

3.3. Age dating

3.3.1. Measurements

Sixty samples including shells and ooids were age dated using AMS radiocarbon following the method from Yokoyama et al. (2019). The best efforts were made to only select pristine grains, unfortunately the extent of meteoric diagenesis often limited choices. Radiocarbon ages were then calibrated on OxCal using Marine20 curve from Heaton et al. (2020) and DeltaR values from Squire et al. (2013). Results, including error ranges, are presented in Table S1.

Five intervals were further investigated using OSL measurements. Ages are calculated by dividing the equivalent dose D_e (Gy), reflecting the radiation absorbed by quartz grains during burial by the dose rate (Gy/ka) of surrounding sediments and cosmic rays (Huntley et al., 1985).

The outer ~1 cm of the samples was removed in red-light conditions. Recovered inner portions were soaked in HCl, H_2O_2, and HF acids and sieved to retain quartz extracts of 180–212 μm diameter. Single quartz grains were stimulated with green (532 nm) laser light (Bøtter-Jensen et al., 2003) for 2 s at 125 °C in a Risø DA20 TL/OSL reader. D_e values were estimated by summing the first 0.1 s of signal and using the final 0.2 s as background following the single-aliquot regenerative-dose (SAR) procedure (Murray and Wintle, 2000). The ultraviolet OSL emission was measured using an Electron Tubes Ltd 9635Q photomultiplier tube fitted with a 7.5 mm Hoya U-340 filter. Laboratory irradiations were obtained using a calibrated 90Sr/90Y beta source.

The suitability of the procedure was tested for each grain using recycling ratio, recuperation (Murray and Wintle, 2000), and OSL-IR (Duller, 2003) depletion ratio tests. The regenerative (220 °C for 10 s) and test dose (220 °C for 10 s) preheat combination was determined using dose-recovery experiments. Such experiment using BB2 material yielded a measured dose ratio of 1.02 ± 0.02 (n = 62), illustrating the accuracy of the procedure. 600 quartz grains were analysed for each sample using numOSL R package (Peng and Li, 2018), the Central Age Model (Galbraith et al., 1999) and Finite Mixture Model (Gliganic et al., 2015; Roberts et al., 2000).

Dose rates were measured using thick-source alpha counting (Guérin et al., 2011), GM-25-5 beta counting corrected for grain-size attenuation (Bøtter-Jensen and Mejdahl, 1988) and an internal quartz dose rate of 0.03 ± 0.01 Gy/ka (Bowler et al., 2003). The cosmic-ray dose rate was calculated following Prescott and Hutton (1994), using a moisture content of 15 ± 5% to allow for past moisture variations during sub-aerial and submerged periods. OSL data are shown in Table S2.

3.3.2. Depth corrections

The measured depths of age-dated samples were corrected to

allow comparison with the RSL curve from Grant et al. (2014), which had been previously deemed applicable to the NWS (Lebrec et al., 2022b). First, subsidence corrections were applied to Freycinet and Paw samples using a base rate of 0.28 mm per year, as measured by Hengesh et al. (2011) in line with previous data from Collins (2002). Considering that the subsidence is regarded as negligible along the continent shoreline (O'Leary et al., 2013), no correction was applied to inner-shelf samples.

Second, all measured depths were corrected for post-depositional compaction following an original approach introduced here. Such corrections are critical because each metre of sediment deposited on the seabed results in an increased compaction of the underlying sedimentary column, until the maximum mechanical compaction is achieved at a depth z_{mmc}, typically between 750 and 1000 m bml (Lee et al., 2021; Scholle and Halley, 1985). As a result, to correct the depositional depth of a palaeo sea-level indicator (e.g., marine terrace) identified at a depth z_{sli} bml, it is necessary to calculate the compaction C generated by sediments x_1 deposited on top of z_{sli} on the underlying sedimentary column. The workflow integrates a compaction trend, in this case from Lee et al. (2021), Eq. (1), to calculate percentage changes in sedimentary column thickness (Eq. (2), i.e. a change in rock volume with a constant spatial extent) and in turn C (Eq. (3)) for any given z_{sli} (Fig. 2).

Considering a sedimentary column *sc* at a time T1 extending from the seabed to the maximum mechanical compaction depth z_{mmc} (Fig. 2, T1), the deposition of x_1 metres of sediment on top of *sc* at T2 shifts the entire compaction profile of *sc* by x_1 metres (Fig. 2, T2). This is equivalent to transferring x_1 metres of sediments from the top to the bottom of *sc* compaction profile. The compaction generated by the accumulation of x_1 metres of sediment therefore corresponds to the difference between the thickness x_1 and the thickness x_2 that x_1 would have below z_{mmc}. The increase in compaction of x_1 can be calculated by first de-compacting x_1 as x_0 to account for the partial compaction occurring between the seabed and z_{sli} and then recompacting it with the maximum compaction rate (Eq. (2)).

$$ø = 55.6^{-z/1331} \tag{1}$$

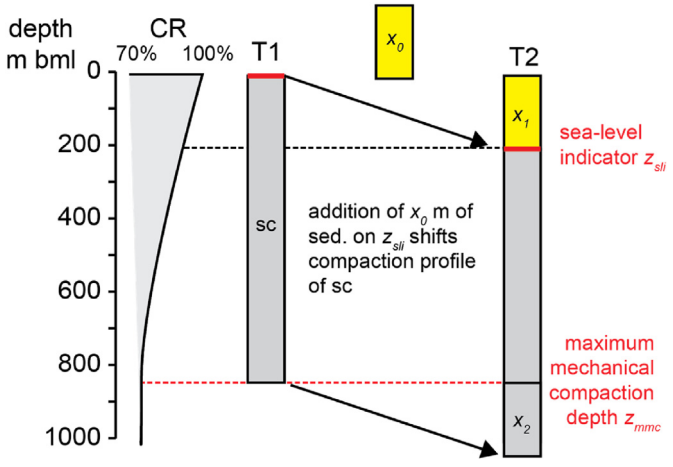

Fig. 2. Compaction corrections for RSL measurements. The accumulation of x_1 metres of sediment on top of a RSL indicator z_{sli} results in an increased compaction of the underlying sedimentary column sc. See text for details.

$$CR = 1 - \frac{ø(0) - ø(z)}{100} \tag{2}$$

$$C = x1 - \frac{x1}{\triangle CR} * CR(z_{mmc}) \; with \; \triangle CR = \frac{\int_{z_{sli}}^{0} (CR)}{x1} \tag{3}$$

where: ø is the sediment porosity (%); z any depth bml (m); CR and $\triangle CR$ the compaction ratio (%); x_1 the thickness of sediments deposited on z_{sli} (m); C the resulting additional compaction (m); z_{sli} the sea-level indicator depth (m); and z_{mmc} the maximum mechanical compaction depth (m).

4. Results

The study is based on the integration of four sites located up to 300 km from each other. To fully capture the depositional and palaeoenvironmental context of each site, we report on them individually, with the exception of Balla Balla and Eighty Miles Beach locations, as these are situated along the same MSLD. For each location, we present the geomorphic features, seismic attributes, sedimentary and diagenetic facies of each sedimentary unit before providing an interpretation of its depositional environment. The description of the sedimentary facies is expended in supplementary material. Sub-sections are then concluded with their respective age models.

4.1. Balla Balla and Eighty Mile Beach ridges

4.1.1. Geomorphic context

The inner shelf is covered with shore-parallel linear ridges that can be tracked almost continuously between Exmouth and Broome (Fig. 1). These ridges are part of the MSLD 20 which includes presumed palaeoshorelines in less than 20 m of water depth (Lebrec et al., 2022b), and are particularly well defined in Balla Balla and Eighty Mile Beach sectors (Fig. 3, A, C).

The nearshore area of Balla Balla is characterised by a tidal embayment enclosed by partly submerged linear ridges (Fig. 3, A). BB1 is located within a tidal pass, on the tip of one of the ridges (Fig. 3, A). Further offshore, BB2 was drilled on the shallowest part of a ridge observed in water depth ranging from 13 to 7.5 m bsl (Fig. 3, A). The ridge extends laterally toward Port Hedland and, while generally parallel to the coast, locally exhibits a seaward progradation associated with meandering channels. Lastly, boreholes BB3, BB4 and BB5 were drilled on a set of ridges that are part of the same prograding trend. Boreholes were positioned on the shallowest ridges, throughout the width of the set (Fig. 3, A).

Along Eighty Mile Beach, EMB2 targeted a ridge located in water depth ranging from 13.2 to 5.4 m bsl. This feature is part of a series of discontinuous ridges that can be followed intermittently between Port Hedland and Broome. Each segment has a length of 2–5 km and can be 10s of kilometres apart from the nearest adjacent segment. Lastly, Boreholes EMB 3 and 4 were drilled at the apex of two set of ridges located in water depths ranging from 15 to 8 m bsl (Fig. 3, C). These ridges are parallel to the modern coast and can be tracked laterally over more than 800 km between the De Grey Delta and Broome. Each ridge is 500 m wide and several meters high.

4.1.2. Sedimentary units

Seven sedimentary units were identified (Fig. 3, B). They are presented hereafter and detailed in Table 2 and Supplementary Material S1.1.

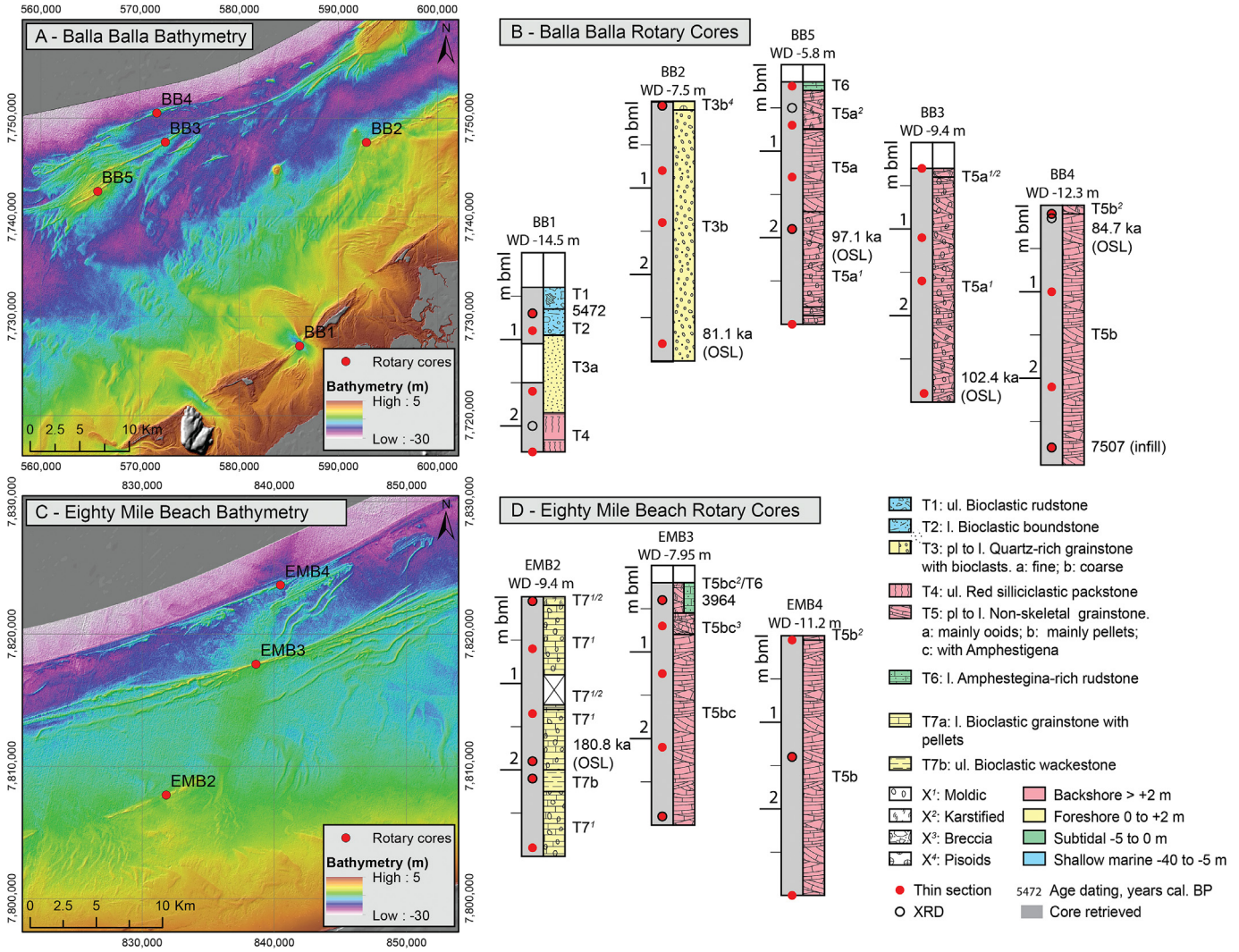

Fig. 3. Location map and synthetic logs of nearshore cores along A-B) Balla Balla and C-D) Eighty Mile Beach. The bathymetry is from Lebrec et al., 2021b and the facies of each sedimentary unit is illustrated in Fig. 4. ul: unlithified; pl: partly lithified; l: lithified.

4.1.2.1. Unit T1 — bioclastic rudstone (shallow marine). This unit is observed at BB1, on the seabed. The sediment, classified as a bioclastic rudstone, is composed of unlithified pebble-size bivalve and coral clasts that are weathered and bioturbated. The interpretation is limited as a significant sand fraction was flushed out during drilling. However, the depth of the tidal channel suggests substantial tidal energy (Fig. 3, A). In this context, this unit is interpreted as accumulated through modern tidal reworking.

4.1.2.2. Unit T2 — bioclastic boundstone (shallow marine to subtidal). Unit T2 is exclusive to BB1. It is composed of pebble-size coral and mollusc clasts, encrusting coralline algae in a matrix of poorly-sorted coarse quartz grains and lithoclasts (Fig. 4, A). There is no evidence that algal grains were reworked and the cement, largely microcrystalline, indicates a shallow marine cementation (James and Jones, 2015; Scholle and Ulmer-Scholle, 2005). It is therefore suggested that coralline algae developed on the hard substrate made of the underlying beachrock, bounding reworked grains.

4.1.2.3. Unit T3 — quartz-rich grainstone with bioclasts (foreshore). The unit is observed at both BB1 (T3a) and BB2 locations (T3b). T3a is a fine-grained, quartz-rich, bioclastic grainstone with feldspars (Fig. 4, B) while T3b consists of a fining-upward coarse-grained quartz-rich bioclastic grainstone.

Unit T3 bioclasts include typical shallow-water open-shelf fauna, such as hyaline and porcelaneous larger benthic foraminifera, as well as a mix of mollusc, echinoderm, bryozoan, planktic foraminifera and green algal debris (Table 2), which have been previously described along the modern NWS (James et al., 2004). The presence of low-angle strata suggests a shoreface to foreshore environment (Short, 2006) which, combined with a fining-upward sequence, is consistent with prograded beachface deposits (Bujan et al., 2019; Davis, 2012; Hunter et al., 1979). Additionally, the combination of both microcrystalline and sparite cements which locally form menisci, as well as the presence of syntaxial cements, illustrate a mixed environment at the interface between the marine and meteoric realm (James and Jones, 2015). Such facies have been previously described in beachrock formed in the upper intertidal zone (Mauz et al., 2015; Vousdoukas et al., 2007). The presence of pisoids at the seabed illustrates significant meteoric weathering after the deposition and cementation of the unit (Calvet and Julià, 1983).

4.1.2.4. Unit T4 — unlithified red siliciclastic packstone (deltaic tidal flat). This unit extends from 1.8 to 2.3 m bml at BB1 location and

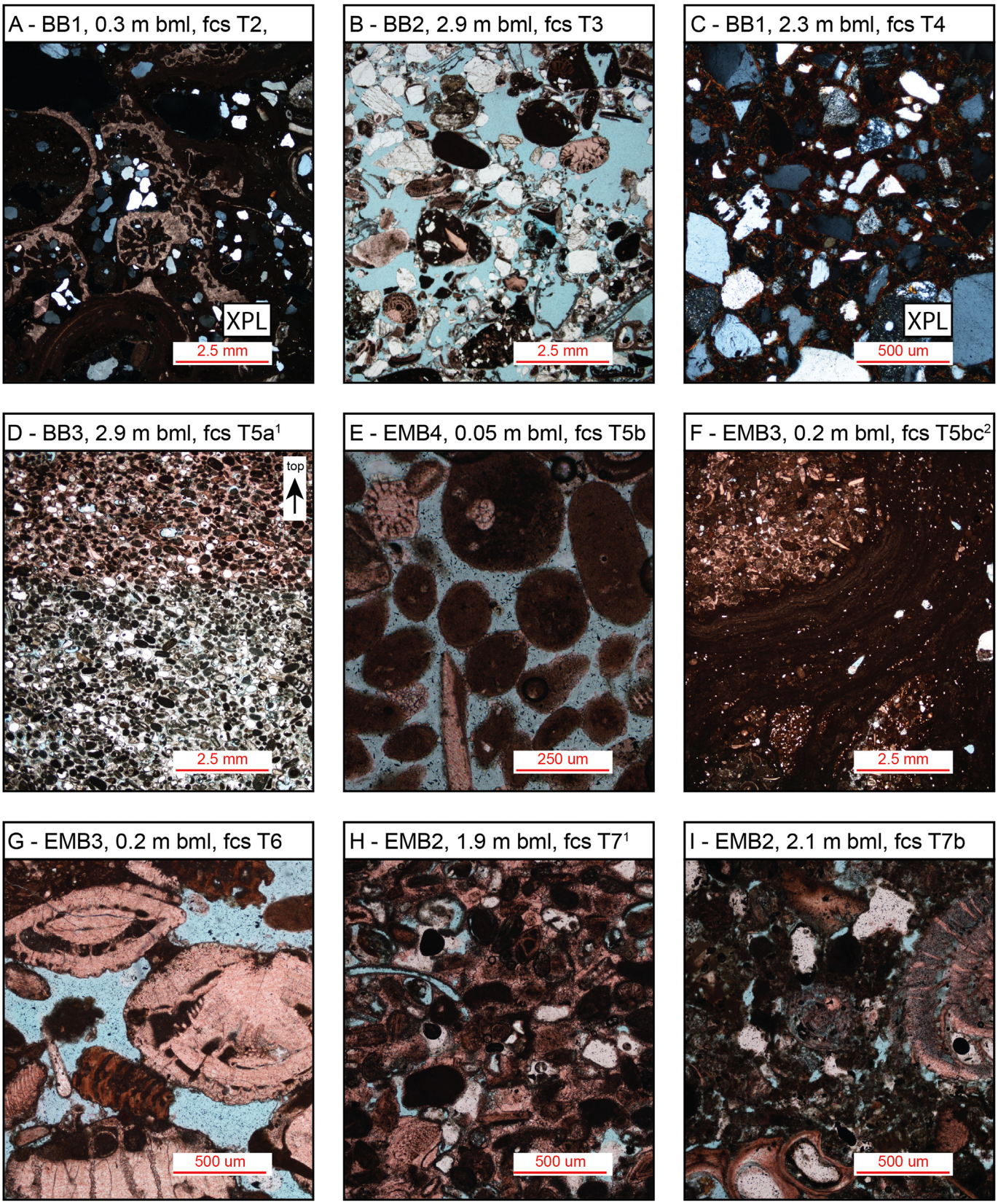

Fig. 4. Balla Balla and Eighty Mile Beach sedimentary units. A) Facies T2, bioclasts and quartz grains encrusted with coralline algae; B) Facies T3, quartz-rich grainstone with bioclasts; C) Facies T4, quartz grains in red clay matrix; D) Facies T5a[1], moldic ooid-rich grainstone showing steep bedding; E) facies T5b, pellet-rich grainstone lithified by meniscus cements; F) Facies T5bc[2], wall of karstified non-skeletal grainstone coated with microcrystalline calcite; G) Facies T6, benthic foraminifera cemented with meniscus-like microcrystalline calcite; H) Facies T7[1], moldic cm-size bioclastic grainstone; I) Facies T7b, bioclastic sand and silt.

Table 2
Balla Balla and Eighty Mile Beach sedimentary units.

Sed. Unit	Name/ Environment	Grains/matrix	Grain size/ sorting	Diagenesis	Structures	XRD (%)
T1	Bioclastic rudstone (shallow marine)	C: mollusc and coral debris.	Pebbles; sediment washed during drilling	Unlithified. Grains appear highly weathered and bioturbated.	Na	Na
T2	Bioclastic boundstone (shallow marine to subtidal)	C: coralline algal, coral and mollusc debris, quartz; F: benthic hyaline foraminifera; R: benthic porcelaneous foraminifera; T: feldspars, bryozoans.	Very fine to granule/ poor	Lithified. Microcrystalline envelops. Pores filled with microcrystalline and equant cements. Dissolution vugs.	Na	Mg calcite (33), Calcite (13.9), Aragonite (22.4), Quartz (22.2), K-Feldspar (8.1), Biotite (<1), Kaolinite (<1)
T3	Quartz-rich grainstone with bioclasts (foreshore)	A: quartz, C: feldspar, F: benthic hyaline (incl. *Amphistegina* and *Operculina*) foraminifera., mollusc and echinoderm debris, R: benthic porcelaneous foraminifera (small miliolids, *Sorites*), coralline algae and bryozoans; T: glauconite, planktic foraminifera, green algae, crustaceans, serpulids.	Fine to coarse/ poor	Partly lithified. Sparite drusy equant cements. Syntaxial cements. Miscroscale alteration. Rare microcrystalline envelops and menisci.	5–10° bedding, fining upward	Calcite (79.7), Quartz (15.5), Aragonite (3.1), Rutile (1.7)
T4	Unlithified red siliciclastic packstone (deltaic tidal flat)	A: quartz; C: feldspars, red clays.	Fine to medium/ moderate	Unlithified.	Na	Quartz (45.7), Calcite (18.6), K-Feldspar (15.4), Albite (14.8), Rutile (1.9), Danalite (1.1), Biotite (1.3), Chlorite & Kaolinite (<1)
T5	Non-skeletal grainstone (backshore)	A: pellets, ooids; F: benthic hyaline foraminifera, echinoderm and mollusc debris; R: quartz, benthic porcelaneous foraminifera; T: feldspars, red algae, planktic foraminifera.	Fine to medium/ well	Lithified. Sparite drusy equant cements. Variably filled pore space. Rare microscale alteration, menisci. Dm dissolution vugs.	30°+ bedding	Calcite (40–95), Aragonite (5–45), Quartz (<1), Halite (<1), T: Pyroxene, Rutile
T6	*Amphistegina*-rich rudstone (subtidal)	A: Corals, coralline algal and benthic hyaline foraminifera (incl. *Amphistegina*) debris; C: mollusc debris; T: bryozoans, crustaceans, undifferentiated foraminifera.	Very coarse to granules/ well	Lithified. Rare microcrystalline envelops, meniscus-type cements, fibrous coating.	Na	Na
T7a	Bioclastic grainstone with pellets (foreshore to backshore)	A: pellets; C: benthic hyaline foraminifera (*Amphistegina* and *Operculina*), echinoderm, mollusc and coralline algal debris; R: ooids, quartz, lithic grains, undifferentiated foraminifera; T: green algae.	Fine to medium/ poor to well	Partly lithified to lithified.	5–10° bedding. Ripples.	Calcite (80–98), Mg calcite (up to 20), Quartz (<1)
T7b	Bioclastic wackestone (foreshore to backshore)	C: Benthic hyaline foraminifera, echinoderm and mollusc debris; F: pellets, quartz; R: ooids, lithic grains, benthic and planktic foraminifera.	Very fine to coarse/ moderate	Unlithified.	Na	Calcite (76.4), Quartz (16.9), Kaolinite (3.4), Biotite (2.2), Chlorite (1.1)

consists of an unlithified mix of fine quartz, feldspar and albite grains in a matrix of calcite and red clays (Fig. 4, C). Similar sediments have been extensively described throughout the Pilbara region as Red Pleistocene Sediments and include alluvial, deltaic and aeolian deposits that form the basement upon which limestone ridges are developed (Hickman and Strong, 2003; Semeniuk, 1992). The cohesivity of the unit T4, the angularity of the quartz grains and the absence of coarse grains suggests that the unit could correspond to a deltaic tidal flat. The interpretation is strengthened by the presence of alluvial fans (*sensu* Miller and Juilleret (2020)) of Red Pleistocene Sediment 10 km landward of the borehole (Semeniuk, 1992).

4.1.2.5. Unit T5 – non-skeletal grainstone (backshore). The unit is a non-skeletal grainstone present at boreholes BB3, BB4, BB5, EMB3 and EMB4 (Fig. 3, B, D). It is possible to discriminate T5a and T5b which contain respectively either mostly surficial ooids (Fig. 4, D) or pellets (Fig. 4, E).

The sedimentary unit T5 presents characteristics typical of aeolian deposits (Table 2) including well-sorted grains with a diameter of less than 2 mm, steep bedding locally in excess of 30°, potential rhizomes (Fig. 4, F) and the lack of macro marine fauna (Frébourg et al., 2008; Hesp, 1988; Loope et al., 2001; Pye and Tsoar, 2009; Vimpere et al., 2022). This interpretation is supported by the diagenetic pattern including sparite menisci, microscale alteration, drusy equant cements, varying infill and porosity inversion that are all specific to meteoric environments (James and Jones, 2015; Moore and Wade, 2013; Scholle and Ulmer-Scholle, 2003). Such observations combined with the seabed morphologies described in Lebrec et al. (2022b) suggest that the unit consists of established (isolated) foredunes and strandplain wind caps developed along Eighty Mile Beach and Balla Balla sectors respectively.

4.1.2.6. Unit T6 - Amphistegina-rich rudstone (subtidal). Unit T6 is present as a plug at the top of BB5 and as a karst infill within EMB3. It consists of *Amphistegina*-rich rudstone with corals (Fig. 4, G).

The unit is characterised by epifauna (including *Amphistegina*, Table 2) commonly found along shallow shelves (Murray, 1991). The location of this unit either on top of lithified aeolianites or within karsts suggests that it was developed following the drowning of the underlying features. Microcrystalline cements which locally form meniscus-like bridges illustrate early shallow-marine microbial cementation in a sub-tidal environment (Diaz and Eberli, 2022; Hillgärtner et al., 2001).

4.1.2.7. Unit T7 – bioclastic grainstone to packstone with pellets (foreshore to backshore). The unit, identified at EMB2 location, consists of a bioclastic grainstone with pellets (Fig. 3, D). Sub units T7a and T7b were discriminated based on their grain-size distributions (Fig. 4, H – I).

The high proportion of hyaline foraminifera associated with epiphytic larger benthic foraminifera such as *Sorites* (soritids) is

indicative of a sediment production along the inner shelf (Beavington-Penney and Racey, 2004; Murray, 1991) which, associated with bedding angles of 5–10°, suggests a deposition in a foreshore environment. The combination of microcrystalline envelopes, characteristic of early marine diagenesis (Ge et al., 2020), with sparite cements, that are usually found in meteoric environments, further restricts the environment to the upper intertidal zone (Mauz et al., 2015). The dimension of the ridge and presence of muddy deposits may illustrate a tidal-flat chenier succession (Augustinus, 1989; Daidu et al., 2013; Hoyt, 1969). Such interpretation is strengthened by the presence of numerous cheniers along the modern coast of Eighty Mile Beach (Semeniuk, 1996, 2008).

4.1.3. Age model

Seven radiocarbon measurements returned age dates varying between 25 ka and 43 ka cal. BP (calibrated age before present, see Supplementary Material for details). Considering that sediments consist of backshore-to-foreshore deposits and that the estimated RSL was about 75 m lower during that time period (Fig. 10), these results likely illustrate post-depositional diagenesis and are therefore invalid. An additional three measurements from karst infills returned age dates varying between 7.5 ka and 4 ka cal. BP representing the drowning of the features following post-LGM sea-level rise.

OSL analyses indicate that quartz grains from BB3 and BB5 were buried during MIS 5c, while those of BB4 and BB2 were buried during MIS 5a (Fig. 10). The presence of early meteoric diagenesis suggests that post-depositional reworking was limited and therefore that the aeolianites BB3, BB4 and BB5 were likely deposited at that time. The age of BB2 is problematic as it appears stratigraphically older than BB3 and BB5 despite a younger OSL age. Such inversion could be the result of the high quartz content of BB2 that may have delayed early cementation and hence facilitated post-depositional reworking, as illustrated by segmented seabed morphologies. It is therefore possible that BB2 was deposited during MIS5d. Along EMB transect, EMB2 returned an OSL age of 180.8 ka +\- 12.7 suggesting an accumulation during early MIS 6. While EMB 3 and 4 could not be dated due to the lack of quartz, the lateral continuity of the aeolianites between Balla Balla and Eighty Miles Beach suggests that they were deposited between MIS 5 d and 5a.

4.2. Paw Ridge

4.2.1. Geomorphic context

The Paw site is centred over a submerged linear ridge located in 70 m of water depth (Fig. 5) that was previously associated with MSLD 90 and 105 (Lebrec et al., 2022b). The ridge has a length of 13 km, a width of 700 m, and, based on high-resolution seismic, a minimum thickness of 75 m (maximum data penetration). All five boreholes are located at the apex of the ridge and within 100 m from each other (Fig. 5). The ridge consists of four superimposed smaller ridges with unresolved internal structures (Fig. 5) that are associated with five sedimentary units (Fig. 6).

4.2.2. Sedimentary units

4.2.2.1. Unit P5 – non-skeletal grainstone (backshore). The lowermost unit extends from a depth of at least 75 m to 50 m bml. In seismic, it consists of two stacked ridges exhibiting a slight progradation. Both ridges are composed of the same sediment, and it was not possible to discriminate them from core observations. The sediment is a non-skeletal grainstone including 70% of pellets and 30% of surficial ooids as well as rare bioclasts (Table 3) and quartz grains (Figs. 6 and 7, I).

The sedimentary unit presents characteristics common to aeolian deposits including well-to-very-well sorted grains with a diameter of less than 2 mm (Frébourg et al., 2008). When visible, bedding angle values appear lower than those reported for typical aeolianites (Loope et al., 2001; McLaren, 2007; Pye and Tsoar, 2009; Vimpere et al., 2022; Yaalon and Laronne, 1971) but are consistent with an established foredune forming mostly through vertical aggradation (Hesp, 1988; Yaalon and Laronne, 1971). This interpretation is supported by the cements. Sparite crystals, variable pore fills, and dissolution of the aragonite are all indicative of meteoric cementation commonly found in association with aeolianites (James and Jones, 2015; Moore and Wade, 2013; Scholle and Ulmer-Scholle, 2003).

4.2.2.2. Unit P4 – coral-rich wackestone to boundstone (shallow marine). The unit is located on the landward part of a 400-m-wide mound, from 50 to 30 m bml (Fig. 5) and is characterised by the presence of corals and coralline algae.

Unit P4 is interpreted as representing the formation of a reefal lagoon and its demise, and is illustrated with five sub-units. The

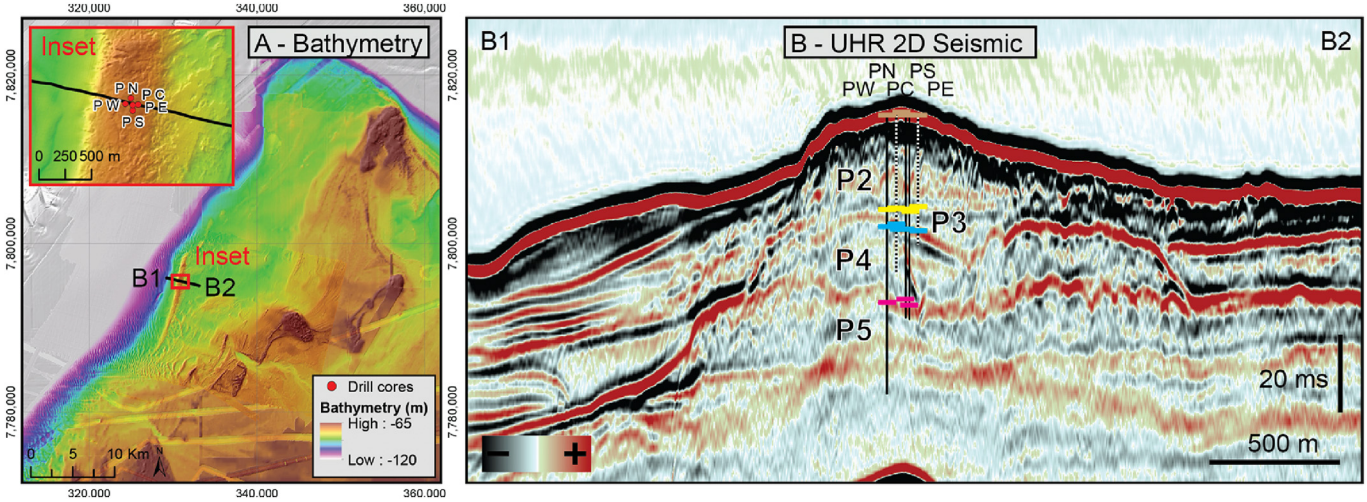

Fig. 5. Paw Ridge morphologies. A) Bathymetry from Lebrec et al., 2021b). B) High-resolution seismic profile courtesy of an industry partner. Synthetic logs are presented in Fig. 6 and the associated facies are illustrated in Fig. 7.

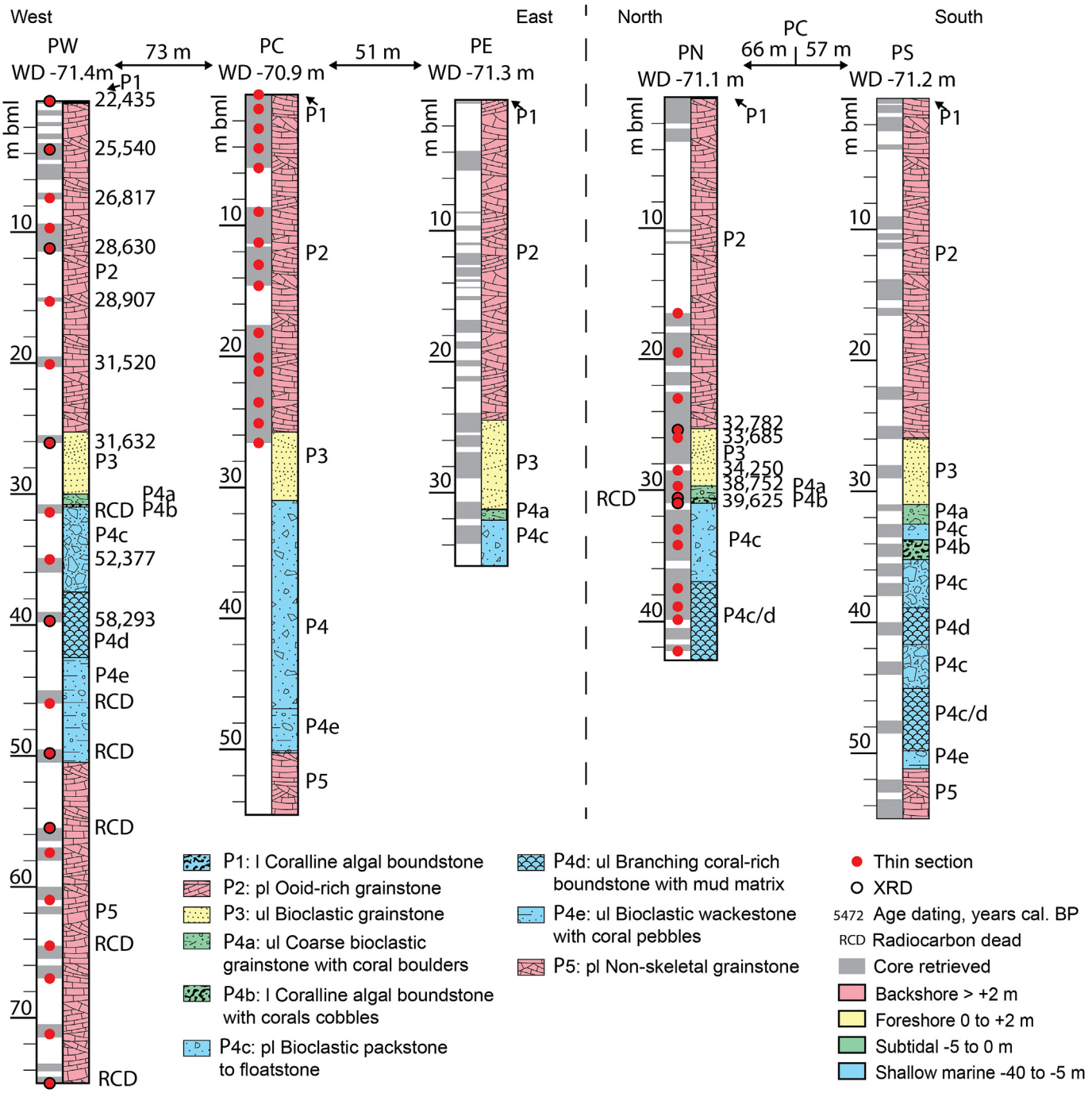

Fig. 6. Paw cores synthetic logs. Core locations and seismic morphologies are displayed in Fig. 5. Sedimentary unit facies are illustrated in Fig. 7.ul: unlithified; pl: partly lithified; l: lithified.

gradual transition from a lithoclasts-dominated to mud-dominated facies throughout the lowermost sub-unit (P4e) highlights the drowning of the substratum and the transition to a protected shoreface environment (Fig. 7, H). The size and distribution of coral branches and encrusting coralline algae found throughout sub-units P4c and P4e (Fig. 7F and G) are consistent with the definition of arborescent corals, known to grow in either protected backreef or forereef environments (Montaggioni, 2005; Montaggioni and Braithwaite, 2009). The position of this unit on the landward side of the mound confirms a backreef environment. The reduction of the lagoon water depth is then illustrated by the presence of 2-m-thick coralline algal crust (P4b, Fig. 7, E) that could represent a reef crest exposed to wave energy (Dean et al., 2015; Montaggioni, 2005; Weiss and Martindale, 2017) and by the identification *homotrema rubrum*, commonly found within reef framework along the NWS (Elliott et al., 1996; Parker and Association of Australasian, 2009). Lastly, the absence of mud and the gradual decrease in reworked coral content within sub-unit P4a (Fig. 7, D) illustrates the transition to a high-energy beach environment.

4.2.2.3. Unit P3 – bioclastic grainstone (foreshore). The sedimentary unit P3 is a bioclastic grainstone (Fig. 7, C) which extends from 30 to

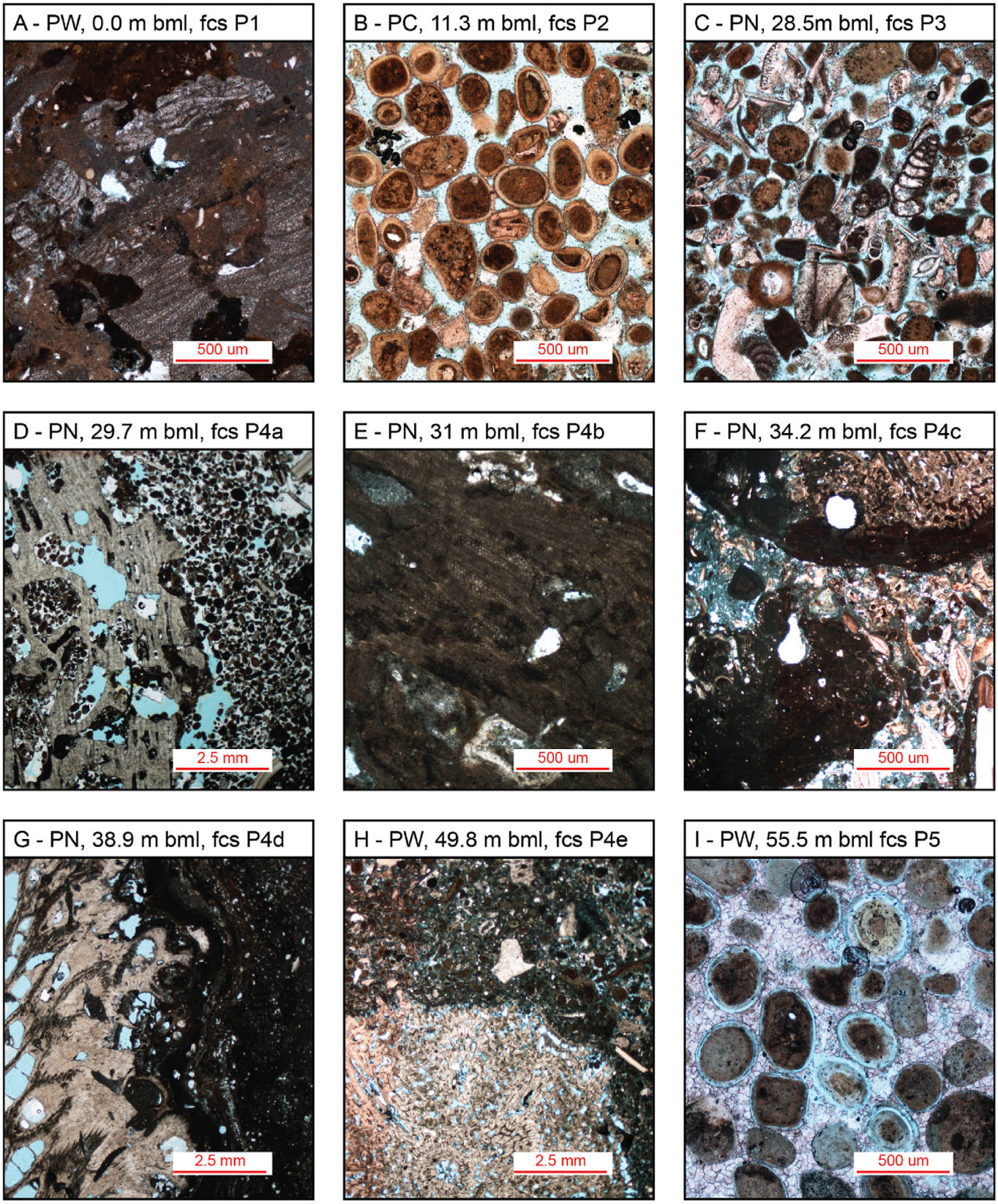

Fig. 7. Paw Ridge sedimentary units. A) Facies P1, coralline algal crust; B) Facies P2, ooid-rich grainstone; C) Facies P3, bioclastic sand; D) Facies P4a, bioclastic graintstone with coral boulders; E) Facies P4b, coralline algal boundstone; F) Facies P4c, coral clasts encrusted with coralline algae in a bioclastic and micropeloidal matrix, and rare quartz grains. G) Facies P4d, branching coral in living position with coralline algal crust. H) Facies P4e, bioclastic wackestone with coral clasts; I) Facies P5, moldic, ooid-rich grainstone lithified with sparry calcite.

Table 3
Paw sedimentary units.

Sed. Unit	Name/ Environment	Grains/matrix	Grain size/ sorting	Diagenesis	Structures	XRD
P1	Coralline algal boundstone (shallow marine)	A: coralline algae; F: mollusc and echinoderm debris; T: quartz, benthic hyaline foraminifera, bryozoan debris.	Na	Lithified.	Na	Na
P2	Ooid-rich grainstone (backshore)	D: ooids; R: benthic hyaline, planktic and porcelaneous foraminifera, mollusc, echinoderm, crustacean and serpulid debris; T: quartz.	Medium/ well	Partly lithified. Equant sparite drusy cements. Partially fill pore space. Ooid cortices often partly dissolved. Syntaxial cements. Rare sparite menisci and microcrystalline envelops.	Bedding 30°+	Aragonite (65–75), Calcite (25–35), Quartz (<1)
P3	Bioclastic grainstone (foreshore)	A: molluscs (bivalve); C: echinoderm, crustacean and coralline algal debris, ooids, pellets; F: benthic hyaline and planktic foraminifera; T: quartz, serpulids, porcelaneous and agglutinated foraminifera.	Fine to medium/ moderate	Unlithified. Some syntaxial and dog teeth cements.	5–10° bedding	Aragonite (35–50), Calcite (15–40), Mg calcite (15–40), Quartz (<1)
P4	Coral-rich wackestone to boundstone (shallow marine)	A: corals, coralline algae; F: mollusc and echinoderm debris, benthic hyaline (incl. encrusting), porcelaneous and planktic foraminifera; R: serpulids, crustaceans.	Fine to gravel	Unlithified. Some corals are filled with fibrous or bladed cements.	Na	Corals: Aragonite (95+); Matrix: Aragonite (25–40), Calcite (25–40), Mg calcite (25–40), Quartz (<1), Dolomite (<1).
P5	Non-skeletal grainstone (backshore)	A: pellets; C: ooids; R: mollusc, echinoderm and crustacean debris, benthic hyaline, porcelaneous and planktic foraminifera; T: quartz.	Fine to medium/ well	Partly lithified. Sparite drusy equant cements fully fills pore space. Most ooids are partly dissolved.	Cross bedding, 20°+	Calcite (50–60), Aragonite (40–50), Halite (<1), Quartz (<1)

26 m bml (Fig. 6) and appears to seal a depression located between the underlying mounds (Fig. 5).

Low-angle inclined strata of varying grain size are typical of beach environments (Bujan et al., 2019; Clifton, 1969; Short, 2006). This interpretation is further supported by the presence of both non-isopachous dog-teeth and syntaxial cements that are common in such environments (Andrieu et al., 2018; Scholle and Ulmer-Scholle, 2003).

4.2.2.4. Unit P2 – ooid-rich grainstone (backshore). The unit P2 corresponds to the linear ridge visible on the seabed (Fig. 5). It is an ooid-rich grainstone (Fig. 7, B), with a few pellets and bioclasts (Table 3), which extends from 26 m bml to the seabed (Fig. 6).

The sedimentary unit is similar to the unit P5 and present characteristics consistent with published descriptions of aeolianites (Frébourg et al., 2008; Hesp, 1988; Loope et al., 2001; McLaren, 2007; Pye and Tsoar, 2009; Scholle and Ulmer-Scholle, 2003; Vimpere et al., 2022; Yaalon and Laronne, 1971). This unit is interpreted, as P5, as a relict established foredune.

4.2.2.5. Unit P1 – coralline algal boundstone (shallow marine). The sedimentary unit P1 is a coralline algal boundstone located on the seabed (Figs. 6 and 7A). The transition with Unit P2 is characterised by multiple dissolution surfaces and borings.

The unit illustrates the growth of coralgal biota on top of a hard substrate following the drowning of the underlying aeolianites. Such growths are common on hard substrates of any origin (Steneck, 1986).

4.2.3. Age model

Paw age model is based on 24 radiocarbon measurements (Figs. 6 and 10, see Supplementary Material for details). Overall, ages increase gradually with depth until the radiocarbon limit is reached, within unit P4. These results indicate that units P4 and P3 were deposited during MIS3, and unit P2 during MIS2. This implies, in turn, that P1, which illustrates the drowning of unit P2, could only be deposited during MIS1. A single age inversion was observed with a sample returning an age of 52 ka within P4a. This inversion reflects the reworked nature of the unit. In the absence of a valid shell radiocarbon age (bulk samples likely captured the age of recrystallisation and are therefore not considered valid) and of quartz grains to conduct OSL dating, the age of unit P5 was determined by comparing the relative position of the unit with respect to published RSL curve through time, corrected for local subsidence and compaction (Fig. 10), suggesting that P5 was likely deposited during MIS 6.

4.3. Freycinet palaeolagoon

4.3.1. Geomorphic context

Freycinet area of interest encompasses a palaeolagoon covering an area of several hundred square kilometres between MSLD 90 and MSLD 105 (Fig. 8, A) associated with barriers, passes and ebb-tidal deltas (Lebrec et al., 2022b). Boreholes are located on the landward border of the lagoon (Fig. 8, B). They have a maximum depth of 48.5 m and intersect 6 sedimentary units (Table 4).

4.3.2. Sedimentary units

4.3.2.1. Unit F6 – bioclastic grainstone (shallow marine). Unit F6 is beyond the penetration of the seismic data. It is intersected at BH1 and BH2 locations from depths of 37.5 m and 39.5 m bml respectively (Fig. 8, D).

The sediment is dominated by a combination of hyaline and porcelaneous calcareous foraminifera (Table 4, Fig. 9, I) that are characteristic of an open-water environment (Murray, 1991). In particular, *Amphistegina*, *Operculina* and *Marginopora* (soritids) are found together along the modern shelf in a water depth of less than 40 m (Haig, 1997; James et al., 2004). The presence of early diagenetic nodules and of micropeloids confirms an accumulation in a shallow-marine environment and a microbial influence (Chafetz, 1986; Macintyre et al., 1985). Lastly, this unit is characterised by the presence of 10% of dolomite. Modern dolomite has been reported in hypersaline and in organic-matter-rich, reducing, environments (Mazzullo, 2000; Mazzullo et al., 1995; Petrash et al.,

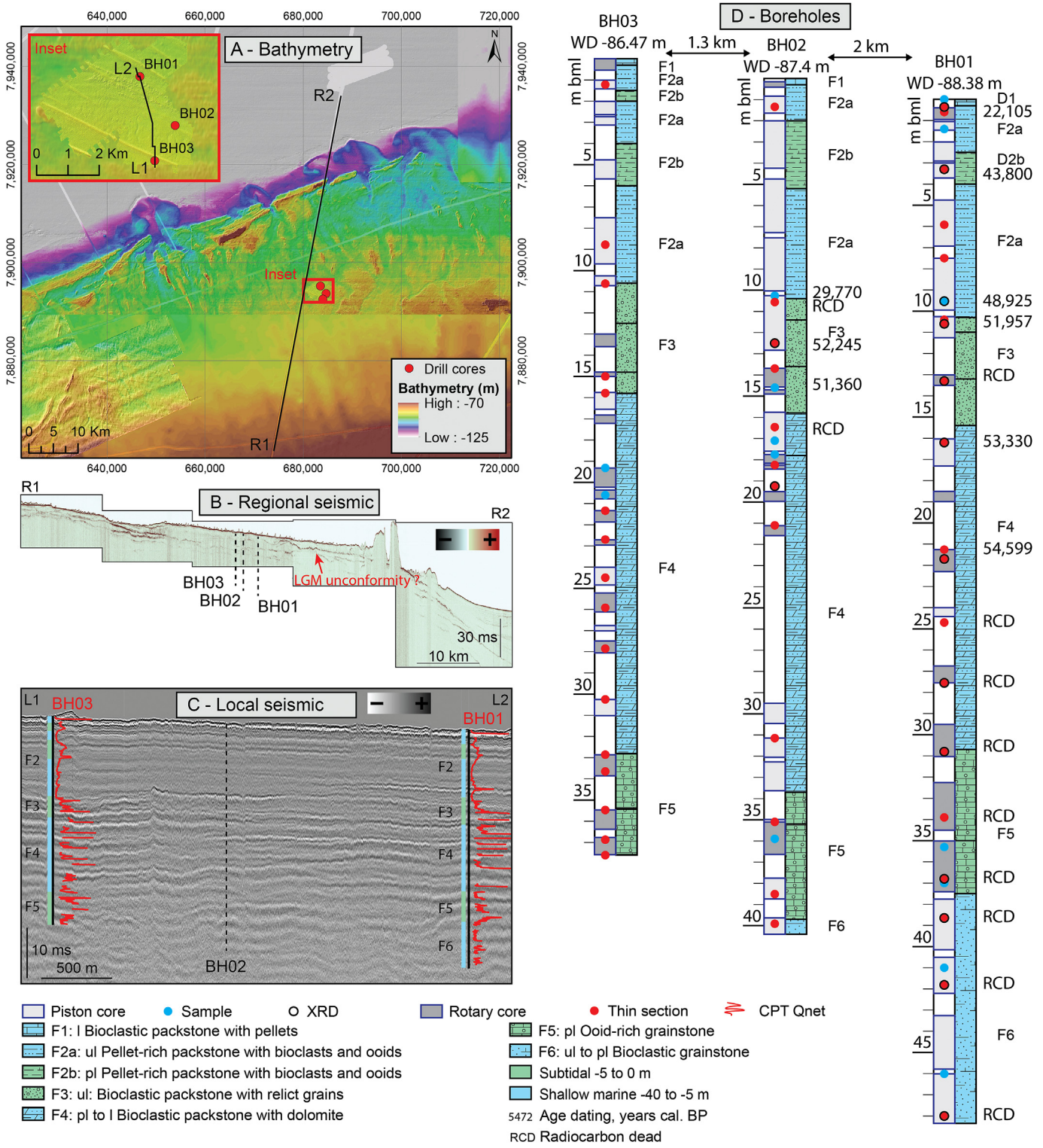

Fig. 8. Morphologies and sedimentary units of Freycinet area. A) Bathymetry, from Lebrec et al., 2021b and derived from data courtesy of TGS. B) Regional 2D Sub-Bottom Profile from Geoscience Australia. C) 2D high-resolution seismic profile and Cone Penetration Tests (CPT) from an industry partner. The colour code corresponds to the main depositional environments. D) Synthetic logs. Facies associated with each sedimentary unit are presented in Fig. 9. ul: unlithified; pl: partly lithified; l: lithified.

2017; Teal et al., 2000; Warren, 2000). Due to the absence of hypersaline lagoonal fauna, the dolomite is interpreted as derived from organodiagenesis.

4.3.2.2. Unit F5 – ooid-rich pack/grainstone (subtidal). The sedimentary unit F5 is intersected at depths ranging from 30.8 to 34.7 m bml and has an average thickness of 6 m (Fig. 8, D). In seismic, the unit is characterised by undulating reflectors which

Table 4
Freycinet palaeolagoon sedimentary units.

Sed. Unit	Name/Environment	Grains/matrix	Grain size/ sorting	Diagenesis	Structures	XRD
F1	Bioclastic packstone with pellets (shallow marine)	C: ooids, pellets, benthic hyaline foraminifera; F: mollusc, echinoderm and bryozoan debris, benthic porcelaneous (small miliolid, *Sorites*) foraminifera; R: planktic foraminifera, bryozoans; T: crutacea, serpulids, green algae.	Medium to granule/ poor	Lithified. Fibrous isopachous cements.	Na	Na
F2	Pellet-rich packstone with bioclasts and ooids (shallow marine to subtidal)	C: ooids, pellets, benthic porcelaneous (small miliolid, *Sorites*, *Peneroplis*, *Alveolinella*) and hyaline foraminifera; F: mollusc, echinoderm and bryozoan debris; T: crutacea, serpulids, green algae, planktic foraminifera, sponge spicules.	Medium to granule/ poor	Unlithified to partly lithified. Microcrystalline meniscus-type cements.	Na	Aragonite (55–85), Calcite (5–10), Mg calcite (10–30), Dolomite (0.5), Quartz (<1)
F3	Bioclastic packstone with relict grains (subtidal)	C: mollusc debris, benthic hyaline (incl. *Amphistegina* and *Operculina*) and porcelaneous (small miliolid, *Sorites*) foraminifera; F: ooids, pellets, echinoderm debris; T: bryozoan, crustaceans, serpulids, planktic foraminifera, green and red algae.	Fine to granule/ moderate	Unlithified to lithified. Microcrystalline meniscus-type cements.	Channels	Calcite (25–50) Aragonite (25–50), Mg calcite (15–25), Dolomite (<1), Quartz (<1), Halite
F4	Bioclastic packstone with dolomite (shallow marine)	A: mollusc and echinoderm debris, benthic hyaline foraminifera (incl. *Amphistegina* and *Operculina*); F: benthic porcelaneous (small miliolid, *Sorites*, *Alveolinella*) foraminifera, bryozoan; R: agglutinated and planktic foraminifera, coralline algae; T: serpulids, crustaceans.	Coarse to granule/ poor	Partly lithified to lithified. Microcrystalline, fibrous, blade and syntaxial cements. Bioclasts partly dissolved.	Na	Calcite (25–35), Mg calcite (25 –35), Aragonite (25–35), Dolomite (10–20), Halite (<1), Quartz (<1), Gypsum (<1), Glauconite (<1)
F5	Ooid-rich pack/ grainstone (subtidal)	A: ooids, pellets; R: benthic hyaline agglutinated and porcelaneous (small miliolid, *Sorites*, *Peneroplis*), mollusc and echinoderm debris; T: crustaceans, serpulids, glauconite.	Medium/ well	Partly lithified to lithified/ microcrystalline to blade cements. Ooids partly dissolved. Molds filled with drusy equant cements. Rare menisci.	Mounds	Calcite (40–85), Aragonite (10 –60), Mg calcite (5), Quartz (<1), Halite (<1)
F6	Bioclastic grainstone (shallow marine)	A: undifferentiated bioclast; C: benthic hyaline foraminifera, echinoderm and mollusc debris; F: planktic foraminifera; T: bryozoans, serpulids, coralline algae, crustaceans, benthic porcelaneous foraminifera.	Medium to granule/ poor	Unlithified to partly lithified. Nodules cemented with fibrous isopachous calcite. Rare syntaxial cements.	Na	Calcite (80–90), Dolomite (10), Aragonite (5–10), Halite (<1) Quartz (<1), Gypsum (<1)

delineate 500-m-wide mounds (Fig. 8, C). The sediment is composed of ooids and pellets but also contains a few bioclasts (Table 4, Fig. 9, G-H).

The presence of ooids, pellets and microcrystalline cements indicates an accumulation and cementation in a very shallow environment (Diaz and Eberli, 2019). The association of *Peneroplis*, *Sorites* and agglutinated foraminifera further suggests a restricted environment (Beavington-Penney and Racey, 2004; Hallock and Glenn, 1986). Similar facies, including microbial filaments and microcrystalline menisci, were described in the modern Bahamas ooid shoals in less than 5 m of water depth (Hillgärtner et al., 2001). The presence of shoals is supported by the mound-like 2D seismic morphology.

4.3.2.3. Unit F4 - bioclastic packstone with dolomite (shallow marine). The unit is intersected at depths varying between 15 and 16 m bml and has a thickness of about 15 m (Fig. 8, D). It is a bioclastic packstone composed dominantly of molluscs, echinoderms and small hyaline foraminifera (Fig. 9, F).

The high proportion of hyaline foraminifera and, to a lesser extent, of porcelaneous foraminifera is characteristic of an accumulation along the inner shelf (Murray, 1991) and of normal marine waters. The presence of isopachous fibrous cements confirms an accumulation and cementation in a shallow marine environment (James and Jones, 2015; Scholle and Ulmer-Scholle, 2003). The amount of mud and micropeloids associated with organic matter suggests a restricted environment (Lakhdar et al., 2006). The presence of dolomite is interpreted as resulting from organodiagenesis (Mazzullo, 2000; Mazzullo et al., 1995; Petrash et al., 2017; Teal et al., 2000). This unit is interpreted as a shallow-water protected environment.

4.3.2.4. Unit F3 – bioclastic packstone with relict grains (subtidal). The unit F3 extends from 10.6 to 15.8 m bml (Fig. 8, D). This sedimentary unit is a pellet-rich packstone with bioclasts and ooids (Fig. 9, E).

The unit includes a mix of molluscs, porcelaneous and hyaline larger benthic foraminifera, echinoderms, bryozoans, planktic foraminifera, green algae and red algae (Table 4), that are characteristic of shallow open marine environments (James et al., 2004; Murray, 1991). This unit is discriminated based on the high percentage of relict grains (>75%), similar to those described along the modern mid shelf (James et al., 2004). The identification of microcrystalline and meniscus-type cements illustrates sub-tidal cementation derived from microbial activity (Diaz and Eberli, 2022; Hillgärtner et al., 2001).

4.3.2.5. Unit F2 – pellet-rich packstone with bioclasts and ooids (shallow marine to subtidal). The unit extends from depths of 0.3 to 10.6 m bml (Fig. 8, D). It is a pellet-rich packstone with bioclasts (Fig. 9, B).

The unit includes pristine miliolids, *Sorites*, *Peneroplis*, alveolinids and *Halimeda* that are principally found in reef environments, and particularly in lagoons (Beavington-Penney and Racey, 2004; Collins et al., 2014; Hallock and Glenn, 1986; Langer, 2000; Murray, 1991). The overlap in depth range and temperature of these grains suggests that the unit was accumulated in less than 15 m of water with temperature varying between 24 °C and 27 °C. The presence of

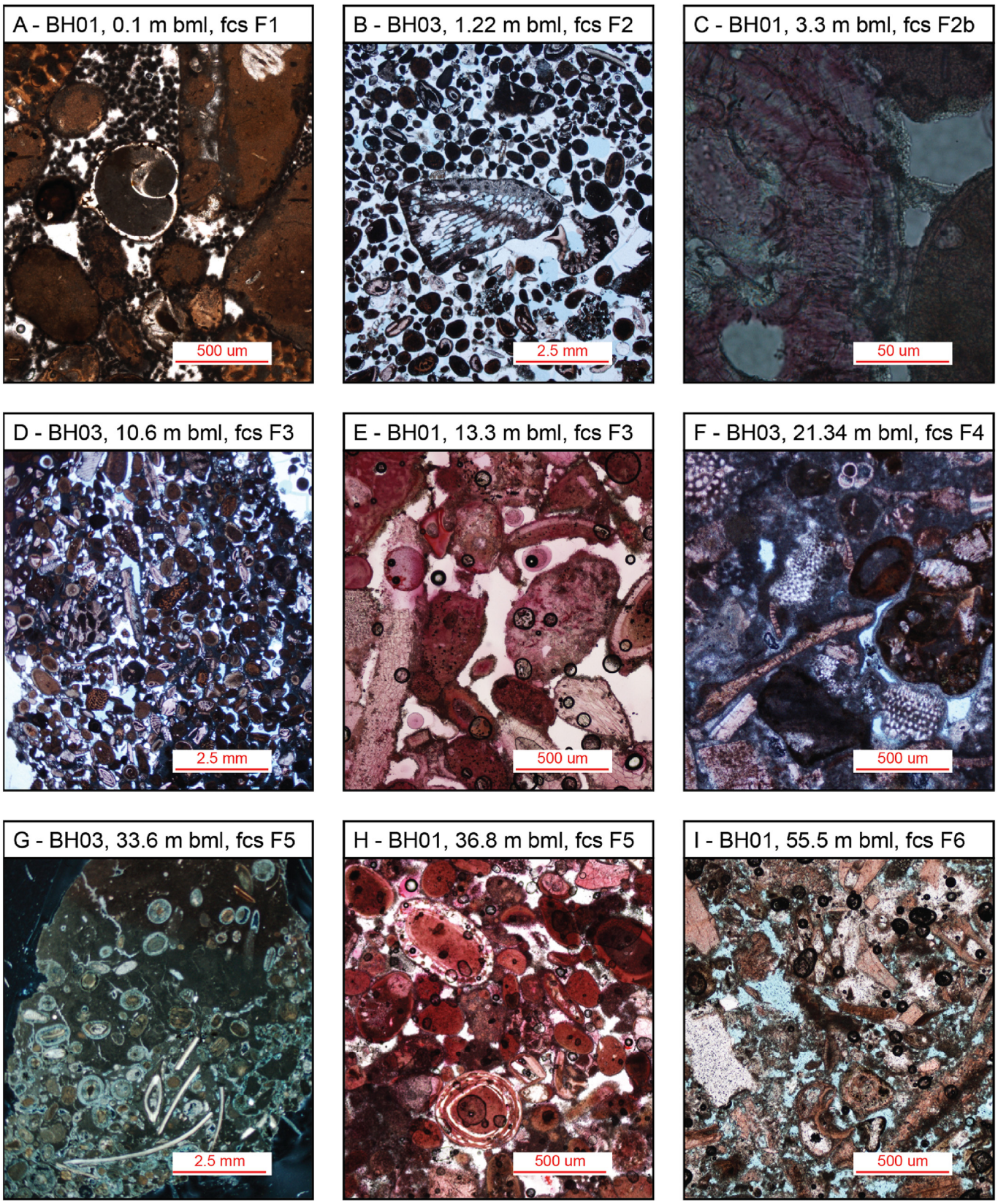

Fig. 9. Freycinet palaeolagoon sedimentary units. A) Facies F1, bioclastic packstone with pellets and micropelloids, cemented by isopachous microcrystalline calcite; B) Facies F2, unlithified pellet-rich packstone; C) Facies F2b, pellets lithified with microcrystalline meniscus-like cement – note the filaments between grains, D) Facies F3, bioclastic grainstone with relict grains; E) Facies F3, locally grains are cemented with meniscus-like microcrystalline calcite; F) Facies F4, bioclasts cemented by isopachous microcrystalline calcite; G) Facies F5, partly dissolved ooids in a muddy matrix; H) Facies F5, partly dissolved ooids cemented with microcrystalline calcite I) Facies F6, bioclastic grainstone.

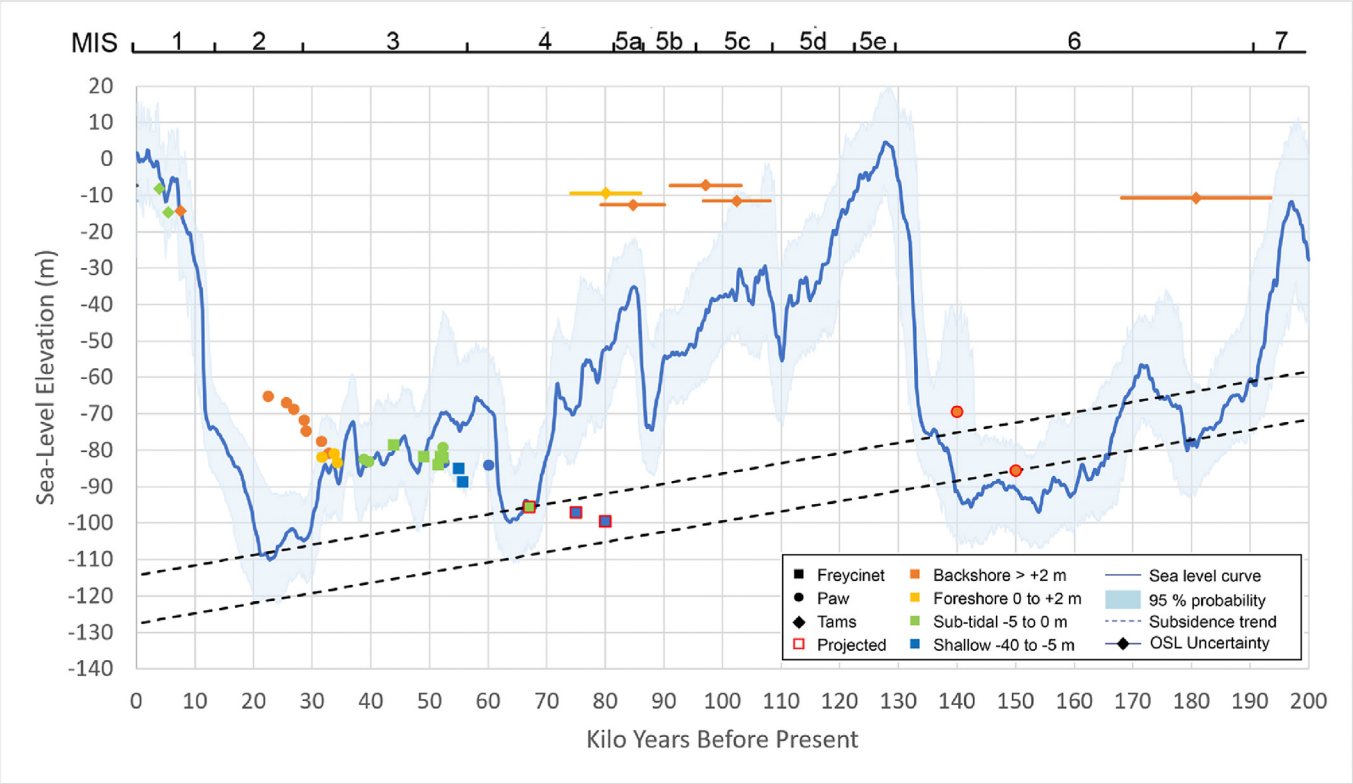

Fig. 10. Age-dated sample palaeodepths, based on p95 cal. BP radiocarbon ages and OSL measurements, corrected for subsidence and compaction. Note that datapoints do not represent RSL measurements but sample corrected depths. RSL curve from Grant et al. (2014). Age dating data, including error estimates are available in Tables S1 and S2.

local layers of firmground associated with microcrystalline meniscus-type cements illustrates intermittent microbial activity, in line with previous studies (Diaz and Eberli, 2022; Hillgärtner et al., 2001).

4.3.2.6. Unit F1 — bioclastic packstone with pellets (shallow marine). The sedimentary unit F1 extends from the seabed to a depth of about 0.3 m bml (Fig. 8, D). This unit, a bioclastic packstone, contains the same grains and bioclasts as the underlying unit F2 (Fig. 9, A).

The increase in planktic foraminifera, associated with a decrease in mud content compared to unit F2 is interpreted as an increase in water depth and/or increased water circulation within the lagoon. The cementation pattern is typical of marine hardground formed in low-sedimentation-rate areas (James and Jones, 2015; Shinn, 1969).

4.3.3. Age model

Radiocarbon measurements were conducted on 24 samples and returned nine dates within ^{14}C range (Figs. 8 and 10, see Supplementary Material for details). Four of them, located within Unit F2 provide conflicting trends with two samples having dates of 43,800 and 48,924 cal. BP and two others of 22,105 and 29,770 years cal. BP. The last two values come from samples associated with recrystallisation. Given that these age dates would place them well above the RSL, they are considered invalid. The three samples from Unit F3 are within a tight age range varying between 51,360 and 52,245 years cal. BP. Lastly, F4 samples returned age dates near ^{14}C maximum range, suggesting that they were deposited during MIS 3. Both units F5 and F6 could not be dated, however the integration of the compaction and of the subsidence with published RSL curves indicates that these units would have been in the right depositional water-depth range during MIS 4 lowstand and highstand respectively (Fig. 10).

5. Discussion

Geotechnical cores from Paw Ridge, Freycinet palaeolagoon, Balla Balla and Eighty Mile Beach areas provide a unique sedimentary archive of the shelf spanning the last 200,000 years. The data support the development of a chronostratigraphic model (section 5.1) and provide insights on the origin and nature of linear ridges along carbonate shelves (section 5.2). This, in turn, illustrates processes controlling carbonate shelf morphologies (section 5.3) as well as the evolution of the climate through eustatic cycles (section 5.4). Additionally, this work provides the basis to develop robust RSL reconstructions through the integration of compaction corrections (section 5.5).

5.1. Shelf chronostratigraphic evolution over the last 200 ka

The integration of the sedimentary units described here, with regional high-resolution seismic data and age dates for coastal landforms, whose measured elevations were corrected for subsidence and compaction, provides insights into the nature of Rowley Shelf palaeoenvironment and RSL variations spanning the last two eustatic cycles (Figs. 10 and 11).

Submerged ridges that were sampled along Balla Balla and Eighty Mile Beach transects were formed between MIS 5c and 5a. These ridges tend to become younger with increasing distance from the coast but share a similar base height of about 17 m bsl, hence

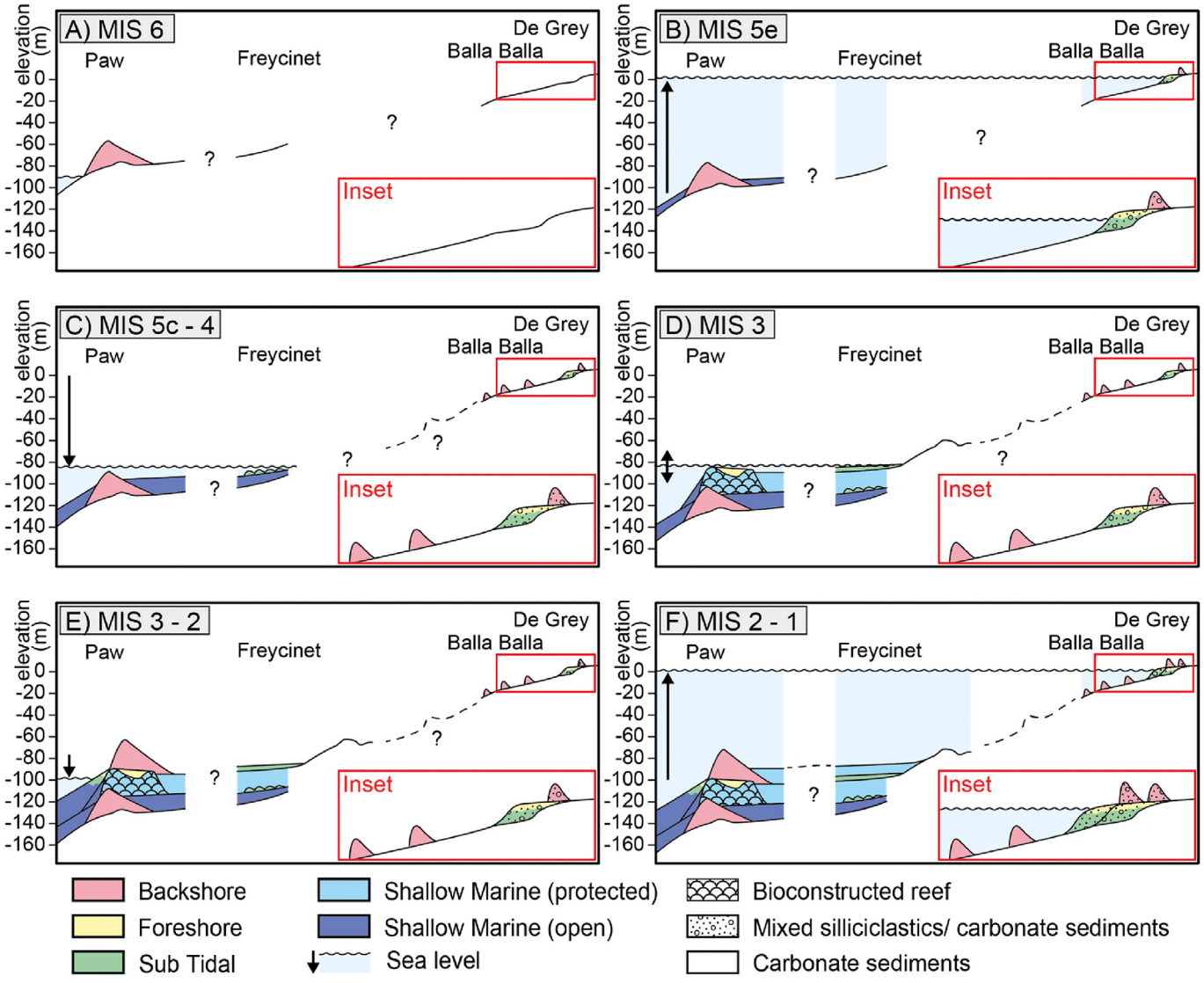

Fig. 11. Chronostratigraphic model of the Rowley Shelf from MIS 6 to present illustrating how the formation of palaeoshorelines (relict coastal ridges) has modified the morphology of the continental shelf. See text for additional details.

illustrating a shoreline regression during MIS 5 and suggesting that MIS 5a and 5c RSLs were similar (Figs. 3 and 11, C). Such features can be followed along the coast over 1100 km (Lebrec et al., 2022b), making them the longest published continuous submerged palaeoshorelines. These features remained exposed during the last glacial period over at least 80,000 years, resulting in the development of karst features. The accumulation of shallow marine and subtidal sediments (Unit T6) within the karsts marks a return to a marine environement following the post LGM sea-level rise (Fig. 11, F). Locally early MIS 6 relict coastal features illustrate antecedent interglacial deposits.

The Paw ridge depositional record spans two glacial-interglacial cycles from MIS 6 to present. The lowermost aeolianite was deposited and cemented during MIS 6 (Unit P5, Fig. 11, A), and was then drowned during the sea-level rise leading to MIS 5 highstand (Fig. 11, C). The ridge remained submerged throughout MIS 5 and 4, but did not record any sedimentation, most likely because sediments, if present, accumulated against its flanks rather than at its apex (Fig. 11, C). MIS 3 sees the development of corals on top of the ridge (Unit P4). The reef and the associated lagoon appear to thrive between 60 and 50 ka before a fall of the RSL led to its demise, characterised by a transition from lagoon to reef flat to beach deposits (Unit P3, Fig. 11, D). The transition to aeolian deposits, at a corrected depth of 80 m below present sea level, suggests an abrupt exposure of the area between 31,632 and 32,782 years cal. BP in line with the termination of MIS 3 (Figs. 10 and 11, E). Aeolian deposits then aggraded throughout MIS 2. The top of the aeolian deposits, dated at 22,435 years cal. BP, would have been located more than 40 m above the RSL reported in Ishiwa et al. (2019a) illustrating substantial vertical accretion. Lastly, following LGM sea-level rise, a thin crust of coralline algae developed on top of the aeolianites (Fig. 11, F) suggesting that the rapid sea-level rise did not allow coral-reef re-establishment, in line with what was observed further North (Webster et al., 2022).

Freycinet site exhibits a similar evolution of the RSL. The barrier enclosing the lagoon appears stratigraphically older than MIS 3 deposits suggesting, based on its resemblance with Paw Ridge, that it could consist of a core of MIS 6 aeolianites. The area would have remained entirely submerged during MIS 5 (Fig. 11, B). The transition from an open shallow-marine environment (<40 m, Unit F6) to

a very shallow shoreface (<5 m, Unit F5) associated with ooid shoals during MIS 4 then illustrates the gradual exposure of the barrier and the renewed closure of the lagoon (Fig. 11, C). The presence of ooid shoals and the absence of terrigenous grains imply, following Diaz and Eberli (2019) and Hallenberger et al. (2019), significant tidal energy and limited fluvial runoff. Then, from 60 to 50 ka, Freycinet site lays in warm shallow water and the preservation of organic matter associated with dolomite indicates a restricted lagoonal environment (Unit F4), similar to the Boujmel lagoon (Lakhdar et al., 2006). The appearance of subtidal reworked sediments associated with erosive channels illustrates a decrease of the RSL (Unit F3). The exact timing of this event is uncertain as most bioclasts are reworked, but they all returned dates between 51,360 and 52,245 years cal. BP, suggesting that this happened shortly after (Figs. 10 and 11, D). Following this initial event, the RSL partially re-established with the accumulation of shallow-lagoonal deposits (Unit F2). The re-appearance of subtidal microbial cements from 43 ka suggests sporadic periods of slightly reduced RSL (Fig. 11, E). MIS 2 deposits were not observed at Freycinet site due to limited core recovery. Nevertheless, regional seismic data exhibit a regional unconformity that intersects Freycinet borehole locations between the seabed and 2 m bml. Overlying sediments appear to fill a regional lagoon associated with an ebb-tidal delta previously described by Lebrec et al. (2022a). Seabed sediments collected from the lagoon were dated between 11 and 14 ka (James et al., 2004) suggesting that the underlying erosive surface could correspond to the LGM (Fig. 11, F). Lastly, the presence of an undated marine hardground at the seabed reflects the post LGM sea-level rise associated with a decrease in sediment supply.

5.2. Origin and nature of carbonate ridges along the Rowley Shelf

Submerged ridges and associated lagoons formed in tropical carbonate-dominated environments such as the NWS, are often interpreted as drowned coral reefs (Gallagher et al., 2014; McCaffrey et al., 2020; Nichol and Brooke, 2011; Vora et al., 1996). Recent improvements of the NWS regional bathymetry led to a re-evaluation of this concept, and revealed that ridges >1000 km long can consist of palaeo-coastal features (Lebrec et al., 2022b). Such interpretation did not include *in-situ* data, hence involving a level of uncertainty. Analysis of the lithology of the drowned ridges and lagoons presented here confirms that those features were dominantly formed through coastal processes.

Indeed, inner-shelf ridges consist of cemented beach deposits and aeolianites, and no indicators of in-place bioconstruction were observed. In fact, the three 1100-km-long linear ridges present along the Rowley Shelf at water depths between 0 and 20 m are interpreted as purely formed by mechanical accumulation of sediments along successive palaeoshorelines. Similarly, Paw Ridge, which is 13 km long and up to 75 m thick (Fig. 5) is composed by 75% of aeolian and beach deposits. The nature of the barrier associated with the lagoon drilled at Freycinet site (Fig. 8A and B) was not ground-truthed. Nevertheless, the lack of coral fragments or coralgal grains in Freycinet boreholes tends to suggest a scarcity of corals and an absence of active bioconstruction during the formation of the lagoon. This might indicate that the Freycinet ridge was also formed by coastal processes, in line with geomorphological interpretations from Lebrec et al. (2022b). However, in the absence of borehole intersecting this ridge, its nature remains speculative.

While those ridges are not bioconstructed, they appear to support local reef development throughout the shelf. This is the case at Paw site, where a MIS 3, 20-m-thick coral reef was identified between two aeolianites, but also along the coastal deposits intersected at Balla Balla and Eighty Mile Beach. Indeed, Lebrec et al. (2022b) reported that these relict coastal deposits are the foundations of modern fringing coral reefs developed along the Rowley Shelf, including Muiron Islands, Montebello Islands, the 64-reef islands, Dampier Archipelago and Bedout Island, hence indicating that relict coastal ridges can control reef spatial distribution. Additionally, each individual aeolianite reported here is thicker than the associated coral-bearing interval and/or has a larger spatial extent, further emphasising that relict coastal features, and not bioconstructed reefs, are the main producers of seafloor ridges along the NWS. Similar patterns, where corals are developed on top of palaeoshorelines deposits, such as aeolianites, are observed offshore Belize, US, Israel, India and South Africa (Droxler and Jorry, 2013; Finkl and Andrews, 2008; Jarrett et al., 2005; Mallarino et al; Ramsay, 1994; Rao et al., 2001). The inter-connectivity between the development of coral reefs and relict coastal features nevertheless implies that the identification of relict coastal features in carbonate domains does not exclude the presence of localised bioconstructed reefs.

5.3. Processes controlling Rowley Shelf morphologies

As previously noted, relict coastal features tend to be concentrated over specific isobaths (Brooke et al., 2017; Lebrec et al., 2022b; Ribo et al., 2020). Given that the RSL changes constantly, it questions what controls such distribution. The first possible explanation is that coastal features form whenever the RSL remains stable long enough to allow their development (Ribo et al., 2020). Such interpretation matches last interglacial RSL curves where each MIS is characterised by a downward RSL plateau (Fig. 10), which would have supported coastal-features development. While this certainly plays a role, it cannot explain all observed morphologies. Some relict coastal features appear to be part of larger composite features that were not entirely formed during the last eustatic cycle. This is notably the case at Paw location, where the seabed ridge is composed of three smaller distinctive features formed during MIS 6, 3, and 2 (Fig. 11).

The influence of pre-existing coastal morphologies on the location of modern deltas and beach ridges has been previously documented along the southeastern african shelf (Engelbrecht et al, 2022) and the De Grey River delta. There, only the most seaward beach ridges formed during the Holocene, and most of the delta 30-km-long seaward progradation was formed during previous eustatic cycles (Lebrec et al., 2023). It is therefore proposed here that shorelines tend to stabilize along pre-existing reliefs until a turning point is achieved (i.e. a specific amount of RSL change required to fully submerge or strand the relief) at which point the shoreline migrates rapidly, before stabilizing against another topographic feature. Each eustatic cycle further emphasizes this pattern resulting in the development of diachronous composite relict coastal features forming distinctive steps or ridges along continental margins, such as the Paw Ridge (Fig. 11, A, D, F). This implies that Rowley Shelf morphologies are controlled by the interaction between RSL, antecedent topography, sediment availability and coastal processes. The main differences between this carbonate shelf and siliciclastic shelves are: (1) the source of the sediments, and (2) the presence of early diagenesis that facilitates coastal features preservation. This has implications for palaeoenvironment studies, as it implies that sedimentary objects that appear to reflect a given chronostratigraphic event (e.g., a seabed ridge) may in fact be composed of diachronous features.

5.4. Evolution of the Rowley Shelf climate

The distribution of the Rowley Shelf relict coastal features illustrates the evolution of the climate, RSL and depositional environments through glacial-interglacial cycles. In particular, it is

possible to observe a shift in palaeocoastal processes between highstand and lowstand periods, with a transition observed in seafloor strata located between 50 and 60 m bsl.

Along the mid-to-outer shelf, lowstand aeolianites formed during glacial periods show heights of up to 25 m. These features are associated with kilometres-wide lagoons and estuaries that can be tracked along the entire coast (Lebrec et al., 2022b; O'Leary et al., 2020). On the contrary, coastal features formed during interglacial periods appear an order of magnitude smaller (Fig. 11, F). Indeed, highstand aeolianites located on the inner shelf show a typical height of about 5 m. Varying exposure time and the associated erosion are not considered to be the primary reason explaining this difference, as these features were preserved through early meteoric cementation. Additionally, the limited number of age inversions observed at Paw and Freycinet sites advocates against significant downslope reworking, and the height of these inner-shelf aeolianites is consistent with modern dunes described along the coast (Semeniuk, 1996, 2008) further suggesting that inner-shelf aeolianites underwent limited post-depositional reworking. Considering that the sediment supply is one of the main controls on foredune height (Davidson-Arnott et al., 2018), these observations suggest that carbonate production was higher during glacial periods. The rate of sea-level change does not appear to affect significantly these observations, as for example MIS 5c and 2 lasted similar durations but are associated with very different depositional heights (5 *versus* 25 m).

In parallel, terrigenous grains appear restricted to highstand interglacial deposits: while inner-shelf cores exhibit up to 45% of quartz, mid-to-outer shelf sites contain a negligible amount of terrigenous grains that rarely exceed 1%. The reduced number of fluvial-influenced features along the mid-to-outer shelf (Lebrec et al., 2022b) suggests that this drop in terrigenous grain content is not solely a relative change driven by an increased carbonate production. Such observations support the previously formulated hypothesis that fluvial runoff increases during interglacial periods, in line with the onset of the monsoon (Hallenberger et al., 2019; Ishiwa et al., 2019b; Kuhnt et al., 2015; Lebrec et al., 2022b). This, in turn, suggests that the spatial interplay between fluvial runoff and carbonate production observed along the continental shelf illustrates a switch-on/switch-off effect of the monsoon across glacial-interglacial cycles.

A shift in dominant coastal processes can also be observed along the coast on either side of the De Grey River. Westward, along the Pilbara coast (Balla Balla), relict coastal features exhibit evidence of fluvial activity in the form of fluvial channels and strandplains, associated with increased quartz content. Such features were not observed eastward, along Eighty Mile Beach, hence illustrating a drier environment. Interestingly this boundary is visible at any water depth as well as along the modern coast (Lebrec et al., 2022b; Semeniuk, 1996, 2008) suggesting that drainage basins and climatic boundaries remained stable across glacial-interglacial cycles.

5.5. RSL reconstruction from submerged palaeoshorelines

RSL reconstructions have been the focus of extensive research over the last decades, as it is a key input for palaeoenvironment and palaeoclimate reconstructions as well as ice-volume estimates (Grant et al., 2012; Grant et al., 2014; Lambeck and Nakada, 1990; Lambeck et al., 2011; Lambeck et al., 2014; O'Leary et al., 2013; Yokoyama et al., 2001; Yokoyama et al., 2006). Over the Quaternary, such reconstructions are largely based on oxygen isotopes and on the identification and age dating of RSL indicators such as corals or palaeoshoreline features, especially in areas that are located far from former ice sheets. In order to integrate individual RSL measurements to generate local RSL curves, measurements are typically corrected for post-depositional vertical displacements stemming from neo-tectonism, subsidence, dynamic topography and glacio-hydro-isostatic effects (Lambeck, 2014). In a review on RSL reconstruction, Lambeck (2014) mentioned that compaction should also be considered. It has however never been properly integrated due to the lack of comparative datasets.

In that context, the recent publication of compaction curves along the NWS (Lee et al., 2021) provided a unique opportunity to study how compaction impacts RSL measurements. The key point is not how the RSL indicator being measured was compacted, but how the overlying deposits compacted the underlying sedimentary column. The method presented here show that, for example, an accumulation of 50 m of sediment results in the compaction of the underlying sedimentary column by 12.74 m. This means that a RSL indicator located 50 m below mud line would have been deposited 12.74 m higher with respect to the RSL. While this number may seem high, it only represents a reduction of the underlying rock volume by 1.5% considering a maximum mechanical compaction depth of 850 m bml.

Based on these results, it is here proposed that compaction corrections should be routinely conducted for RSL indicators. This approach should not be limited to buried RSL indicators: outcropping indicators may have been buried at some points, therefore resulting in some level of compaction that needs to be accounted for. In addition, the use of a simplified equation (Eq. (4)), that only requires theoretical maximum compaction ratio values, which on the NWS corresponds to 0.74, returns induced compaction values similar to these obtained using site-specific data (12.74 vs 13.21 m with a burial of 50 m) further promoting the integration of such corrections.

$$C = x1 - x1 * CR(z_{mmc}) \quad (4)$$

where C is the compaction, $x1$ the depth of a sea-level indicator and $CR(z_{mmc})$ the maximum mechanical compaction ratio.

This novel approach has a number of limitations. First, it is based on an average compaction rate along the shelf, that is assuming that lithology changes will balance each other along the sedimentary column, and may not be representative of local lithology variations. Second, erosive events will be characterised by a jump in the compaction values that will impact the maximum mechanical compaction depth. Such patterns are already included in empirical compaction curves and therefore only affect theoretical models. Lastly, the proposed method considers that sediments are burying uniformly RSL indicators (e.g., 50 m of sediments being deposited over the entire shelf), but in the case of coastal deposits, sediments will tend to accumulate at specific locations (e.g., a foredune). It would therefore be necessary to investigate how localised loads impact compaction trends.

6. Conclusion

The NWS is a low-angle carbonate platform stretching over 2400 km along the tropical northwestern Australia. Previous studies identified numerous linear ridges along the shelf, stacked along nine modal sea level depths (MSLDs) between the modern shoreline and the 140 m isobath. However, due to the limited extent of publicly available data, the nature of these features remained elusive. The integration of geotechnical cores scattered across the shelf in water depth ranging from 5 to 90 m bsl, with newly processed geophysical data and an extensive age-dating program, provided a unique opportunity to investigate the origin and nature of these ridges and to delve into processes controlling carbonate shelf morphologies across eustatic cycles.

The study was concentrated over four sites of interest. Balla

Balla and Eighty Miles Beach transects investigated a series of submerged linear ridges that can be tracked over more than 1100 km between Exmouth and Broome along MSLD 20 m. These ridges were formed during the last two interglacial periods and have characteristics typical of aeolianites and beachrocks, making them the longest continuous submerged relict coastal features described to date. Further offshore, wide barriers associated with lagoons, estuaries, ebb-tidal deltas and beach ridges form distinctive morphologies along both MSLD 90 m and 105 m. Paw cores, located on the apex of one of these barriers, reveal that they are mainly composed of stacked MIS 6 and MIS 2 aeolianites that can individually reach thicknesses in excess of 25 m. Interestingly, Paw MIS 6 aeolianites provided the substrate for the development of a 20-m-thick MIS 3 bioconstructed reef, that became itself the substratum for the development of the MIS 2 aeolianites. The absence of coral fragments from Freycinet barrier-lagoon system, located 200 km eastward, suggests that such reefal development was localised and confirms that MSLD 105 and 90 ridges are dominantly formed of relict coastal deposits.

As shown here, MSLD ridges are composed of stacked diachronous relict coastal features formed through multiple eustatic cycles that can reach tens of metres in height and extend over hundreds of kilometres. As the RSL varies, shorelines stabilize along existing topographic features until sufficient variations break the equilibrium, at which point the shoreline migrates rapidly before stabilizing against another feature, hence reinforcing further a step-like pattern at each cycle. Coral reefs, where present, are developed on top of these features, reproducing their morphologies, but only have a limited impact on the Rowley Shelf regional shelf morphologies. On that basis it is suggested that Rowley Shelf morphologies are controlled by the distribution of relict coastal features that are themselves controlled by the interaction between RSL, sediment availability, coastal processes, antecedent topography and most critically early diagenesis which dictates which features can be preserved.

Lastly, the mineralogy, size and distribution of relict coastal features provide insights on the shelf palaeoenvironments. First, the modern climatic boundary between the arid riverine Pilbara and sediment-starved Canning coasts is observed at all water depths, suggesting that it remains stable through glacial/interglacial cycles. Additionally, along the Rowley Shelf, terrigenous grains content and fluvial morphologies prominence reduce with increasing water depth while, at the same time, carbonate production increases. Such asymmetry is expected to reflect the onset of the monsoon during interglacial periods resulting in increased fluvial runoff and reduced carbonate precipitation.

These results confirm that the submerged linear ridges of the Rowley Shelf are dominantly relict coastal features formed through wave, tidal, fluvial and wind processes. On that basis, special care should be taken when interpreting geophysical morphologies in carbonate-dominated environments. Indeed, ridge morphologies tens of metres thick, and >1000 km long, can consist of relict coastal features. At the same time, the identification of coastal morphologies does not exclude the presence of local bioconstructed intervals.

The development of the chronostratigraphic framework was further supported by the integration of compaction corrections. Such corrections are critical because the accumulation of sediments on top of a RSL indicator compacts the underlying sedimentary column, therefore affecting RSL measurements. The deposition of 50 m of sediment can generate nearly 13 m of compaction suggesting that compaction corrections should be commonly investigated as part of RSL reconstructions and chronostratigraphic studies in a similar way to glaci-hydro isostatic and subsidence corrections.

Authorship declaration

Ulysse Lebrec: Conceptualization, Methodology, Investigation, Formal analysis, Data curation, Writing – original draft, Funding acquisition. **Rosine Riera**: Formal analysis, Writing – original draft. **Mic**hael **O'Leary**: Supervision, Writing – review & editing, Funding acquisition. **Jody Webster**: Supervision, Writing – review & editing, Validation. **Yusuke Yokoyama**: Investigation, Formal analysis, Writing – review & editing. **Luke Gliganic**: Investigation, Formal analysis, Writing – review & editing. **Simon C. Lang**: Supervision, Resources, Writing – review & editing. **Victorien Paumard**: Resources, Writing – review & editing

Declaration of competing interest

The authors declare that they have no known competing financial interests or personal relationships that could have appeared to influence the work reported in this paper.

Data availability

Data will be made available on request.

Acknowledgments

The authors are indebted to the Norwegian Geotechnical Institute, The Robson Robertson is an award from UWA Ocean Institute: https://www.uwa.edu.au/oceans-institute/Engage/Funding-and-grants. The University of Western Australia and the Geological Society of Australia for supporting the project. Additionally, many thanks are due to TAMS Group for performing nearshore coring. The authors are grateful to Phil Watson, TGS and the Centre for Energy and Climate Geoscience industry partners for providing proprietary data. The authors are thankful to ESRI and IHS Markit for licensing ArcGIS software and IHS Kingdom respectively. Lastly, the authors would like to thank two anonymous reviewers and Ingrid Hendy for respectively reviewing and handling the manuscript.

Appendix A. Supplementary data

Supplementary data to this article can be found online at https://doi.org/10.1016/j.quascirev.2023.108164.

References

Abdul Wahab, M.A., Radford, B., Cappo, M., Colquhoun, J., Stowar, M., Depczynski, M., Miller, K., Heyward, A., 2018. Biodiversity and spatial patterns of benthic habitat and associated demersal fish communities at two tropical submerged reef ecosystems. Coral Reefs 37, 327–343.

Ahr, W.M., 1973. Carbonate ramp—alternative to shelf model. AAPG (Am. Assoc. Pet. Geol.) Bull. 57 (9), 1826, 1826.

Ahr, W.M., 1998. Carbonate Ramps, 1973–1996: a Historical Review. Geological Society. Special Publications, London, pp. 7–14, 149(1).

Andrieu, S., Brigaud, B., Barbarand, J., Lasseur, E., 2018. The complex diagenetic history of discontinuities in shallow-marine carbonate rocks: new insights from high-resolution ion microprobe investigation of δ18O and δ13C of early cements. Sedimentology 65 (2), 360–399.

Aston, C., Langlois, T., Fisher, R., Monk, J., Gibbons, B., Giraldo-Ospina, A., Lawrence, E., Keesing, J., Lebrec, U., Babcock, R.C., 2022. Recreational fishing impacts in an offshore and deep-water marine park: examining patterns in fished species using hybrid frequentist model selection and bayesian inference. Front. Mar. Sci. 9.

Augustinus, P.G.E.F., 1989. Cheniers and chenier plains: a general introduction. Mar. Geol. 90 (4), 219–229.

Australian Institute of Marine Science, 2022. NWSSRP Theme 2 - Project 2a: Characterising the Ancient Coastline Key Ecological Feature (KEF). Australian Institute of Marine Science (AIMS).

Baines, P.G., 1981. Satellite observations of internal waves on the Australian northwest shelf. Mar. Freshw. Res. 32 (3), 457–463.

Baker, C., Potter, A., Tran, M., Heap, A.D., 2008. Sedimentology and Geomorphology of the Northwest Marine Region of Australia. Geoscience Australia, Canberra, p. 220. Record 2008/7.
Beavington-Penney, S.J., Racey, A., 2004. Ecology of extant nummulitids and other larger benthic foraminifera: applications in palaeoenvironmental analysis. Earth Sci. Rev. 67 (3), 219–265.
Beemer, R., Bandini-Maeder, A., Shaw, J., Lebrec, U., Cassidy, M., 2018. The Granular Structure of Two Marine Carbonate Sediments, ASME 2018 37th International Conference on Ocean. Offshore and Arctic Engineering, Madrid, Spain, p. 11.
Belde, J., Reuning, L., Back, S., 2017. Bottom currents and sediment waves on a shallow carbonate shelf, Northern Carnarvon Basin, Australia. Continent. Shelf Res. 138, 142–153.
Benjamin, J., O'Leary, M., McDonald, J., Wiseman, C., McCarthy, J., Beckett, E., Morrison, P., Stankiewicz, F., Leach, J., Hacker, J., Baggaley, P., Jerbic, K., Fowler, M., Fairweather, J., Jeffries, P., Ulm, S., Bailey, G., 2020. Aboriginal artefacts on the continental shelf reveal ancient drowned cultural landscapes in northwest Australia. PLoS One 15 (7), e0233912.
Bonesso, J.L., Cuttler, M.V.W., Browne, N., Hacker, J., O'Leary, M., 2020. Assessing reef island sensitivity based on LiDAR-derived morphometric indicators. Rem. Sens. 12 (18), 3033.
Bosence, D., 2005. A genetic classification of carbonate platforms based on their basinal and tectonic settings in the Cenozoic. Sediment. Geol. 175 (1), 49–72.
Bøtter-Jensen, L., Andersen, C.E., Duller, G.A.T., Murray, A.S., 2003. Developments in radiation, stimulation and observation facilities in luminescence measurements. Radiat. Meas. 37 (4), 535–541.
Bøtter-Jensen, L., Mejdahl, V., 1988. Assessment of beta dose-rate using a GM multicounter system. Int. J. Radiat. Appl. Instrum. Nucl. Tracks Radiat. Meas. 14 (1), 187–191.
Bowler, J.M., Johnston, H., Olley, J.M., Prescott, J.R., Roberts, R.G., Shawcross, W., Spooner, N.A., 2003. New ages for human occupation and climatic change at Lake Mungo, Australia. Nature 421 (6925), 837–840.
Braje, T.J., Maloney, J.M., Gusick, A.E., Erlandson, J.M., Nyers, A., Davis, L., Gill, K.M., Reeder-Myers, L., Ball, D., 2019. Working from the known to the unknown: linking the subaerial archaeology and the submerged landscapes of santarosae island, alta California, USA. Open Quat. 5, 1–15.
Brooke, B.P., Nichol, S.L., Huang, Z., Beaman, R.J., 2017. Palaeoshorelines on the Australian continental shelf: morphology, sea-level relationship and applications to environmental management and archaeology. Continent. Shelf Res. 134, 26–38.
Bujan, N., Cox, R., Masselink, G., 2019. From fine sand to boulders: examining the relationship between beach-face slope and sediment size. Mar. Geol. 417, 106012.
Burchette, T.P., Garland, J., Neilson, J.E., Laubach, S.E., Whidden, K.J., 2012. Carbonate Rocks and Petroleum Reservoirs: a Geological Perspective from the Industry, Advances in Carbonate Exploration and Reservoir Analysis. Geological Society of London, p. 0.
Burchette, T.P., Wright, V.P., 1992. Carbonate ramp depositional systems. Sediment. Geol. 79 (1), 3–57.
Calvet, F., Julià, R., 1983. Pisoids in the Caliche Profiles of Tarragona. Springer Berlin Heidelberg, Berlin, Heidelberg, pp. 456–473. N.E. Spain.
Carrigy, M.A., Fairbridge, R.W., 1954. Recent sedimentation physiography and structure of the continental shelves of western Australia. J. Roy. Soc. West Aust. 38, 65–95.
Cathro, D.L., Karner, G.D., 2006. Cretaceous–Tertiary inversion history of the Dampier Sub-basin, northwest Australia: insights from quantitative basin modelling. Mar. Petrol. Geol. 23 (4), 503–526.
Chafetz, H.S., 1986. Marine peloids; a product of bacterially induced precipitation of calcite. J. Sediment. Res. 56 (6), 812–817.
Clifton, H.E., 1969. Beach lamination: nature and origin. Mar. Geol. 7 (6), 553–559.
Collins, L., 2002. Tertiary foundations and quaternary evolution of coral reef systems of Australia's North West Shelf. In: Moss, S.J., Keep, M. (Eds.), The Sedimentary Basins of Western Australia 3. Petroleum Exploration Society of Australia, Perth, Western Australia, pp. 129–152.
Collins, L.B., James, N.P., Bone, Y., Chiocci, F.L., Chivas, A.R., 2014. Carbonate Shelf Sediments of the Western Continental Margin of Australia, Continental Shelves of the World: Their Evolution during the Last Glacio-Eustatic Cycle. Geological Society of London, p. 0.
Currey-Randall, L.M., Galaiduk, R., Stowar, M., Vaughan, B.I., Miller, K.J., 2021. Mesophotic fish communities of the ancient coastline in Western Australia. PLoS One 16 (4), e0250427.
Daidu, F., Yuan, W., Min, L., 2013. Classifications, sedimentary features and facies associations of tidal flats. J. Palaeogeogr. 2 (1), 66–80.
Davidson-Arnott, R., Hesp, P., Ollerhead, J., Walker, I., Bauer, B., Delgado-Fernandez, I., Smyth, T., 2018. Sediment budget controls on foredune height: comparing simulation model results with field data. Earth Surf. Process. Landforms 43 (9), 1798–1810.
Davis, R.A.J., 2012. Coastal Sedimentary Environments. Springer, New York.
Dean, A., Steneck, R., Tager, D., Pandolfi, J., 2015. Distribution, abundance and diversity of crustose coralline algae on the Great Barrier Reef. Coral Reefs 34.
Diaz, M.R., Eberli, G.P., 2019. Decoding the mechanism of formation in marine ooids: a review. Earth Sci. Rev. 190, 536–556.
Diaz, M.R., Eberli, G.P., 2022. Microbial contribution to early marine cementation. Sedimentology 69 (2), 798–822.
Dix, G.R., 1989. High-energy, inner shelf carbonate facies along a tide-dominated non-rimmed margin, northwestern Australia. Mar. Geol. 89 (3), 347–362.
Dix, G.R., James, N.P., Kyser, T.K., Bone, Y., Collins, L.B., 2005. Genesis and dispersal of carbonate mud relative to late quaternary sea-level change along a distally-steepened carbonate ramp (northwestern shelf, western Australia). J. Sediment. Res. 75 (4), 665–678.
Driscoll, N.W., Karner, G.D., 1998. Lower crustal extension across the Northern Carnarvon basin, Australia: evidence for an eastward dipping detachment. J. Geophys. Res. Solid Earth 103 (B3), 4975–4991.
Droxler, A.W., Jorry, S.J., 2013. Deglacial origin of barrier reefs along low-latitude mixed siliciclastic and carbonate continental shelf edges. Ann. Rev. Mar. Sci 5 (1), 165–190.
Duller, G.A.T., 2003. Distinguishing quartz and feldspar in single grain luminescence measurements. Radiat. Meas. 37 (2), 161–165.
Dunham, R.J., Ham, W.E., 1962. Classification of Carbonate Rocks According to Depositional Texture1, Classification of Carbonate Rocks—A Symposium. American Association of Petroleum Geologists, p. 0.
Elliott, J.M., Logan, A., Thomas, M.L.H., 1996. Morphotypes of the foraminiferan homotrema rubrum (lamarck): distribution and relative abundance on reefs in Bermuda. Bull. Mar. Sci. 58, 261–276.
Embry, A.F., Klovan, J.E., 1971. A late Devonian reef tract on northeastern banks island, N.W.T.1. Bull. Can. Petrol. Geol. 19 (4), 730–781.
Engelbrecht, L.D., Green, A.N., Cooper, J.A.G., Mackay, C.F., 2022. Antecedent geological control on transgressive delta and shoreline preservation: Examples from the SE African shelf. Marine Geology 454, 106934.
Finkl, C.W., Andrews, J.L., 2008. Shelf geomorphology along the southeast Florida atlantic continental platform: barrier coral reefs, nearshore bedrock, and morphosedimentary features. J. Coast Res. 244, 823–849.
Folk, R.L., Ward, W.C., 1957. Brazos River bar [Texas]; a study in the significance of grain size parameters. J. Sediment. Res. 27 (1), 3–26.
Frébourg, G., Hasler, C.-A., Le Guern, P., Davaud, E.J., 2008. Facies characteristics and diversity in carbonate eolianites. Facies 54, 175–191.
Friedman, G.M., 1985. The term micrite or micritic cement is a contradiction; discussion of micritic cement in microborings is not necessarily a shallow-water indicator; discussion. J. Sediment. Res. 55 (5), 777, 777.
Galbraith, R.F., Roberts, R.G., Laslett, G.M., Yoshida, H., Olley, J.M., 1999. Optical dating of single and multiple grains of quartz from Jinmium rock shelter, northern Australia: part I: experimental design and statistical models. Archaeometry 41 (2), 339–364.
Gallagher, S., Fulthorpe, C.S., Bogus, K., Auer, G., Baranwal, S., Castañeda, I., Christensen, B., De Vleeschouwer, D., Franco, D., Groeneveld, J., Gurnis, M., Haller, C., He, Y., Henderiks, J., Himmler, T., Ishiwa, T., Iwatani, H., Jatiningrum, R., Kominz, M., Zhang, W., 2017. Expedition 356 Methods.
Gallagher, S.J., Reuning, L., Himmler, T., Henderiks, J., De Vleeschouwer, D., Groeneveld, J., Lari, A.R., Fulthorpe, C.S., Bogus, K., 2018. The enigma of rare Quaternary oolites in the Indian and Pacific Oceans: a result of global oceanographic physicochemical conditions or a sampling bias? Quat. Sci. Rev. 114–122.
Gallagher, S.J., Wallace, M.W., Hoiles, P.W., Southwood, J.M., 2014. Seismic and stratigraphic evidence for reef expansion and onset of aridity on the Northwest Shelf of Australia during the Pleistocene. Mar. Petrol. Geol. 57, 470–481.
Ge, Y., Lokier, S.W., Hoffmann, R., Pederson, C.L., Neuser, R.D., Immenhauser, A., 2020. Composite micrite envelopes in the lagoon of Abu Dhabi and their application for the recognition of ancient firm- to hardgrounds. Mar. Geol. 423, 106141.
Gealy, E.L., Winterer, E.L., Moberly Jr., R.M., 1971. Methods, Conventions, and General Observations. Initial Reports of the Deep Sea Drilling Project Covering Leg 7 of the Cruises of the Drilling Vessel Glomar Challenger. Guam to Honolulu, Apra, p. 9. Hawaii, August-September 1969.
Gliganic, L.A., May, J.H., Cohen, T.J., 2015. All mixed up: using single-grain equivalent dose distributions to identify phases of pedogenic mixing on a dryland alluvial fan. Quat. Int. 362, 23–33.
Grant, K.M., Rohling, E.J., Bar-Matthews, M., Ayalon, A., Medina-Elizalde, M., Bronk Ramsey, C., Satow, C., Roberts, A.P., 2012. Rapid coupling between ice volume and polar temperature over the past 150,000 years. Nature (London) 491 (7426), 744–747.
Grant, K.M., Rohling, E.J., Bronk Ramsey, C., Cheng, H., Edwards, R.L., Florindo, F., Heslop, D., Marra, F., Roberts, A.P., Tamisiea, M.E., Williams, F., 2014. Sea-level variability over five glacial cycles. Nat. Commun. 5 (1), 5076, 5076.
Griffith, J., 2004. Scleractinian corals collected during 1998 from the dampier Archipelago, western Australia. Record West Aust. Mus. 66, 101–120. Supplement.
Guérin, G., Mercier, N., Adamiec, G., 2011. Dose-rate conversion factors: update. Ancient TL 29, 5–8.
Haig, D., 1997. Foraminifera from Exmouth Gulf. Western Australia.
Hallenberger, M., Reuning, L., Back, S., Gallagher, S.J., Iwatani, H., Lindhorst, K., 2022. Climate and sea-level controlling internal architecture of a Quaternary carbonate ramp (Northwest Shelf of Australia). Sedimentology 69 (3), 1276–1300. https://doi.org/10.1111/sed.12948.
Hallenberger, M., Reuning, L., Gallagher, S.J., Back, S., Ishiwa, T., Christensen, B.A., Bogus, K., 2019. Increased fluvial runoff terminated inorganic aragonite precipitation on the Northwest Shelf of Australia during the early Holocene. Sci. Rep. 9 (1), 18356.
Hallock, P., Glenn, E.C., 1986. Larger foraminifera: a tool for paleoenvironmental analysis of cenozoic carbonate depositional facies. Palaios 1 (1), 55–64.
Hearty, P., O'Leary, M., Donald, A., Lachlan, T., 2006. The enigma of 3400 years BP coastal oolites in tropical northwest Western Australia… why then, why there? Sediment. Geol. 186 (3–4), 171–185.
Heaton, T.J., Köhler, P., Butzin, M., Bard, E., Reimer, R.W., Austin, W.E.N., Bronk

Ramsey, C., Grootes, P.M., Hughen, K.A., Kromer, B., Reimer, P.J., Adkins, J., Burke, A., Cook, M.S., Olsen, J., Skinner, L.C., 2020. Marine20—the marine radiocarbon age calibration curve (0–55,000 cal BP). Radiocarbon 62 (4), 779–820.
Hengesh, J., Whitney, B., Rovere, A., 2011. A Tectonic Influence on Seafloor Stability along Australia's North West Shelf, the Twenty-First International Offshore and Polar Engineering Conference. Maui, Hawaii, USA, pp. 596–604.
Hesp, P., 1988. Morphology, dynamics and internal stratification of some established foredunes in southeast Australia. Sediment. Geol. 55 (1), 17–41.
Hesse, P.P., Magee, J.W., van der Kaars, S., 2004. Late Quaternary climates of the Australian arid zone: a review. Quat. Int. 118, 87–102.
Hickman, A., Strong, C., 2003. Dampier – Barrow Island, W. A., second ed. Geological Survey of Western Australia.
Hillgärtner, H., Dupraz, C., Hug, W., 2001. Microbially induced cementation of carbonate sands: are micritic meniscus cements good indicators of vadose diagenesis? Sedimentology 48 (1), 117–131.
Holloway, P.E., 1995. Leeuwin current observations on the Australian North West Shelf, may–june 1993. Deep Sea Res. Oceanogr. Res. Pap. 42 (3), 285–305.
Holloway, P.E., 2001. A regional model of the semidiurnal internal tide on the Australian North West Shelf. J. Geophys. Res.: Oceans 106 (C9), 19625–19638.
Hoyt, J.H., 1969. Chenier versus barrier, genetic and stratigraphic Distinction1. AAPG (Am. Assoc. Pet. Geol.) Bull. 53 (2), 299–306.
Hunter, R.E., Clifton, H.E., Phillips, R.L., 1979. Depositional processes, sedimentary structures, and predicted vertical sequences in barred nearshore systems, southern Oregon coast. J. Sediment. Res. 49 (3), 711–726.
Huntley, D.J., Godfrey-Smith, D.I., Thewalt, M.L.W., 1985. Optical dating of sediments. Nature 313 (5998), 105–107.
International Society of Soil Mechanics and Geotechnical Engineering, 2005. Geotechnical & Geophysical Investigations for Offshore and Nearshore Developments. International Society for Soil Mechanics and Geotechnical Engineering.
Ishiwa, T., Yokoyama, Y., Okuno, J.i., Obrochta, S., Uehara, K., Ikehara, M., Miyairi, Y., 2019a. A sea-level plateau preceding the Marine Isotope Stage 2 minima revealed by Australian sediments. Sci. Rep. 9 (1), 6449.
Ishiwa, T., Yokoyama, Y., Reuning, L., McHugh, C.M., De Vleeschouwer, D., Gallagher, S.J., 2019b. Australian Summer Monsoon variability in the past 14,000 years revealed by IODP Expedition 356 sediments. Prog. Earth Planet. Sci. 6.
James, N.P., Bone, Y., Kyser, T.K., Dix, G.R., Collins, L.B., 2004. The importance of changing oceanography in controlling late Quaternary carbonate sedimentation on a high-energy, tropical, oceanic ramp: north-western Australia. Sedimentology 51 (6), 1179–1205.
James, N.P., Jones, B., 2015. Origin of Carbonate Sedimentary Rocks. Wiley.
James, N.P., Mountjoy, E.W., Stanley, D.J., Moore, G.T., 1983. Shelf-Slope Break in Fossil Carbonate Platforms: an Overview1, the Shelfbreak: Critical Interface on Continental Margins. SEPM Society for Sedimentary Geology, p. 0.
Jarrett, B.D., Hine, A.C., Halley, R.B., Naar, D.F., Locker, S.D., Neumann, A.C., Twichell, D., Hu, C., Donahue, B.T., Jaap, W.C., Palandro, D., Ciembronowicz, K., 2005. Strange bedfellows—a deep-water hermatypic coral reef superimposed on a drowned barrier island; southern Pulley Ridge, SW Florida platform margin. Mar. Geol. 214 (4), 295–307.
Jones, A.T., Kennard, J.M., Logan, G.A., Grosjean, E., Marshall, J., 2009. Fluid expulsion features associated with sand waves on Australia's central North West Shelf. Geo Mar. Lett. 29 (4), 233–248.
Jones, H.A., 1973. Marine Geology of the Northwest Australian Continental Shelf. Department of Minerals and Energy, Bureau of Mineral resources, geology and geophysics, p. 117.
Katsumata, K., 2006. Tidal stirring and mixing on the Australian North West Shelf. Mar. Freshw. Res. 57 (3), 243–254.
Keep, M., Harrowfield, M., Crowe, W., 2007. The neogene tectonic history of the North West West Shelf, Australia. Explor. Geophys. 38 (3), 151–174.
Khorshid, M.S., 1990. Development of Geotechnical Experience on the North West Shelf, E.H.Davis Memorial Lecture. Australian Geomechanics, p. 11.
Kordi, M.N., Collins, L.B., O'Leary, M., Stevens, A., 2016. ReefKIM: an integrated geodatabase for sustainable management of the kimberley reefs, north west Australia. Ocean Coast Manag. 119, 234–243.
Kuhnt, W., Holbourn, A., Xu, J., Opdyke, B., De Deckker, P., Röhl, U., Mudelsee, M., 2015. Southern Hemisphere control on Australian monsoon variability during the late deglaciation and Holocene. Nat. Commun. 6 (1), 5916.
Lakhdar, R., Soussi, M., Ben Ismail, M.H., M'Rabet, A., 2006. A Mediterranean Holocene restricted coastal lagoon under arid climate: case of the sedimentary record of Sabkha Boujmel (SE Tunisia). Palaeogeogr. Palaeoclimatol. Palaeoecol. 241 (2), 177–191.
Lambeck, K., 2014. Glacio(hydro)-Isostatic Adjustment, pp. 1–8.
Lambeck, K., Nakada, M., 1990. Late Pleistocene and Holocene sea-level change along the Australian coast. Palaeogeogr. Palaeoclimatol. Palaeoecol. 89 (1), 143–176.
Lambeck, K., Purcell, A., Flemming, N.C., Vita-Finzi, C., Alsharekh, A.M., Bailey, G.N., 2011. Sea level and shoreline reconstructions for the Red Sea: isostatic and tectonic considerations and implications for hominin migration out of Africa. Quat. Sci. Rev. 30 (25), 3542–3574.
Lambeck, K., Rouby, H., Purcell, A., Sun, Y., Sambridge, M., 2014. Sea level and global ice volumes from the last glacial maximum to the Holocene. Proc. Natl. Acad. Sci. USA 111 (43), 15296–15303.
Langer, M., 2000. Biogeography of selected larger foraminifera. Micropaleontology 46, 105–126.
Laugié, M., Michel, J., Pohl, A., Poli, E., Borgomano, J., 2019. Global distribution of modern shallow-water marine carbonate factories: a spatial model based on environmental parameters. Sci. Rep. 9 (1), 16432.
Lebrec, U., Lang, S.C., Paumard, V., O'Leary, M., Yokoyama, Y., Hacker, J., Webster, J., 2023. Discovery of Holocene Ooid Shoals in a Siliciclastic Delta. De Grey River, North West Shelf, Australia. Geology.
Lebrec, U., Paumard, V., O'Leary, M.J., Lang, S.C., 2021b. Towards a regional high-resolution bathymetry of the North West Shelf of Australia based on Sentinel-2 satellite images, 3D seismic surveys, and historical datasets. Earth Syst. Sci. Data 13 (11), 5191–5212.
Lebrec, U., Riera, R., Paumard, V., Leary, M.J., Lang, S.C., 2022a. Automatic mapping and characterisation of linear depositional bedforms: theory and application using bathymetry from the North West West Shelf of Australia. Rem. Sens. 14 (2), 280.
Lebrec, U., Riera, R., Paumard, V., O'Leary, M.J., Lang, S.C., 2022b. Morphology and distribution of submerged palaeoshorelines: insights from the North West West Shelf of Australia. Earth Sci. Rev. 224, 103864.
Lee, E.Y., Kominz, M., Reuning, L., Gallagher, S.J., Takayanagi, H., Ishiwa, T., Knierzinger, W., Wagreich, M., 2021. Quantitative compaction trends of Miocene to Holocene carbonates off the west coast of Australia. Aust. J. Earth Sci. 68 (8), 1149–1161.
Longhurst, A.R., Pauly, D., Longhurst, A.R., Pauly, D., 1987. Chapter 2 - Geography of the Tropical Oceans, Ecology of Tropical Oceans. Academic Press, San Diego, pp. 5–26.
Loope, D.B., Abegg, F.E., Abegg, F.E., Loope, D.B., Harris, P.M., 2001. Recognition and Geologic Preservation of Ancient Carbonate Eolianites, Modern and Ancient Carbonate Eolianites: Sedimentology, Sequence Stratigraphy, and Diagenesis. SEPM Society for Sedimentary Geology, p. 0.
Macintyre, I.G., Schneidermann, N., Harris, P.M., 1985. Submarine Cements—The Peloidal Question, Carbonate Cements: Based on a Symposium Sponsored by the Society of Economic Paleontologists and Mineralogists. SEPM Society for Sedimentary Geology, p. 0.
Mallarino, G., Francis, J.M., Jorry, S.J., Daniell, J.J., Droxler, A.W., Dickens, G.R., Beaufort, L., Bentley, S.J., Opdyke, B.N., Peterson, L.C., 2021. Timescale dependent sedimentary record during the past 130 kyr from a tropical mixed siliciclastic-carbonate shelf edge and slope: Ashmore Trough (southern Gulf of Papua). Sedimentology 68 (6), 2606–2648. https://doi.org/10.1111/sed.12867.
Mauz, B., Hijma, M.P., Amorosi, A., Porat, N., Galili, E., Bloemendal, J., 2013. Aeolian beach ridges and their significance for climate and sea level: concept and insight from the Levant coast (East Mediterranean). Earth Sci. Rev. 121, 31–54.
Mauz, B., Vacchi, M., Green, A., Hoffmann, G., Cooper, A., 2015. Beachrock: a tool for reconstructing relative sea level in the far-field. Mar. Geol. 362, 1–16.
Mazzullo, S.J., 2000. Organogenic dolomitization in peritidal to deep-sea sediments. J. Sediment. Res. 70 (1), 10–23.
Mazzullo, S.J., Bischoff, W.D., Teal, C.S., 1995. Holocene shallow-subtidal dolomitization by near-normal seawater, northern Belize. Geology 23 (4), 341–344.
McCaffrey, J.C., Wallace, M.W., Gallagher, S.J., 2020. A cenozoic Great barrier reef on Australia's North West Shelf. Global Planet. Change 184, 103048.
McLaren, S.J., 2007. Aeolianite, Geochemical Sediments and Landscapes, pp. 149–172.
Miller, B.A., Juilleret, J., 2020. The colluvium and alluvium problem: historical review and current state of definitions. Earth Sci. Rev. 209, 103316.
Montaggioni, L.F., 2005. History of Indo-Pacific coral reef systems since the last glaciation: development patterns and controlling factors. Earth Sci. Rev. 71 (1), 1–75.
Montaggioni, L.F., Braithwaite, C.J.R., 2009. Quaternary Coral Reef Systems : History, Development Processes and Controlling Factors. Elsevier Science Ltd., Amsterdam Burlington, Mass.
Montaggioni, L.F., Cabioch, G., Thouveny, N., Frank, N., Sato, T., Sémah, A.-M., 2011. Revisiting the Quaternary development history of the western New Caledonian shelf system: from ramp to barrier reef. Mar. Geol. 280 (1), 57–75.
Moore, C.H., Wade, W.J., 2013. Carbonate Reservoirs : Porosity and Diagenesis in a Sequence Stratigraphic Framework. Elsevier Science, Amsterdam ; New York.
Moustaka, M., Mohring, M., Holmes, T., Evans, R., Thomson, D., Nutt, C., Stoddart, J., Wilson, S., 2019. Cross-shelf heterogeneity of coral assemblages in northwest Australia. Diversity 11 (2), 15.
Mueller, R.J., 2015. Evidence for the biotic origin of seabed pockmarks on the Australian continental shelf. Mar. Petrol. Geol. 64, 276–293.
Multer, H.G., Gischler, E., Lundberg, J., Simmons, K.R., Shinn, E.A., 2002. Key largo limestone revisited: Pleistocene shelf-edge facies, Florida keys, USA. Facies 46 (1), 229–271.
Murray, A.S., Wintle, A.G., 2000. Luminescence dating of quartz using an improved single-aliquot regenerative-dose protocol. Radiat. Meas. 32 (1), 57–73.
Murray, J.W., 1991. Ecology and Palaeoecology of Benthic Foraminifera. Longman Scientific & Technical.
Nichol, S.L., Brooke, B.P., 2011. Shelf habitat distribution as a legacy of Late Quaternary marine transgressions: a case study from a tropical carbonate province. Continent. Shelf Res. 31 (17), 1845–1857.
O'Leary, M.J., Hearty, P.J., Thompson, W.G., Raymo, M.E., Mitrovica, J.X., Webster, J.M., 2013. Ice sheet collapse following a prolonged period of stable sea level during the last interglacial. Nat. Geosci. 6 (9), 796–800.
O'Leary, M.J., Paumard, V., Ward, I., 2020. Exploring Sea Country through high-resolution 3D seismic imaging of Australia's NW shelf: resolving early coastal landscapes and preservation of underwater cultural heritage. Quat. Sci. Rev.

239, 106353.
Parker, J.H., Association of Australasian, P., 2009. Taxonomy of Foraminifera from Ningaloo Reef, Western Australia. Association of Australasian Palaeontologists.
Peng, J., Li, B., 2018. Single-aliquot Regenerative-Dose (SAR) and Standardised Growth Curve (SGC) Equivalent Dose Determination in a Batch Model Using the R Package 'numOSL', vol. 35.
Petrash, D.A., Bialik, O.M., Bontognali, T.R.R., Vasconcelos, C., Roberts, J.A., McKenzie, J.A., Konhauser, K.O., 2017. Microbially catalyzed dolomite formation: from near-surface to burial. Earth Sci. Rev. 171, 558–582.
Prescott, J.R., Hutton, J.T., 1994. Cosmic ray contributions to dose rates for luminescence and ESR dating: large depths and long-term time variations. Radiat. Meas. 23 (2), 497–500.
Purcell, P.G., Purcell, R.R., 1988. The North West shelf, Australia, an introduction. In: Purcell, P.G., Purcell, R.R. (Eds.), North West Shelf Symposium. Petroleum Exploration Society of Australia, Perth, W.A, pp. 4–15.
Purkis, S., Kerr, J., Dempsey, A., Calhoun, A., Metsamaa, L., Riegl, B., Kourafalou, V., Bruckner, A., Renaud, P., 2014. Large-scale carbonate platform development of Cay Sal Bank, Bahamas, and implications for associated reef geomorphology. Geomorphology 222, 25–38.
Purkis, S.J., Harris, P.M., 2016. The extent and patterns of sediment filling of accommodation space on Great bahama bank. J. Sediment. Res. 86 (4), 294–310.
Pye, K., Tsoar, H., 2009. Aeolian Sand and Sand Dunes. Springer-Verlag Berlin Heidelberg.
Ramsay, P.J., 1994. Marine geology of the sodwana bay shelf, southeast Africa. Mar. Geol. 120 (3), 225–247.
Rao, K.M., Murthy, K.S.R., Reddy, N.P.C., Subrahmanyam, A.S., Lakshminarayana, S., Rao, M.M.M., Sarma, K.V.L.N.S., Premkumar, M.K., Sree, A., Bapuji, M., 2001. Submerged beach ridge lineation and associated sedentary fauna in the innershelf of Gopalpur coast, Orissa, Bay of Bengal. Curr. Sci. 81 (7), 828–833.
Ribo, M., Goodwin, I.D., O'Brien, P., Mortlock, T., 2020. Shelf sand supply determined by glacial-age sea-level modes, submerged coastlines and wave climate. Sci. Rep. 10 (1), 462.
Riera, R., Lebrec, U., Lang, S.C., Paumard, V., 2023. Differentiating Reefal Ridges from Relict Coastal Ridges: Lessons from the Seismic Geomorphologic Study of Buried Miocene Buildups. North West Shelf, Australia (in press). Basin Research, n/a(n/a).
Riera, R., Paumard, V., de Gail, M., Saqab, M.M., Lebrec, U., Lang, S.C., Lane, A., 2022. Origin of seafloor pockmarks overlying submarine landslides: insights from semi-automated mapping of 3D seismic horizons (North West Shelf, Australia). Mar. Petrol. Geol. 136, 105453.
Roberts, R.G., Galbraith, R.F., Yoshida, H., Laslett, G.M., Olley, J.M., 2000. Distinguishing dose populations in sediment mixtures: a test of single-grain optical dating procedures using mixtures of laboratory-dosed quartz. Radiat. Meas. 32 (5), 459–465.
Romine, K., Durrant, J., Cathro, D., Bernardel, G., 1997. Petroleum play element prediction for the cretaceous-tertiary basin phase, northern carnarvon basin. The APPEA Journal 37, 315–339.
Scholle, P.A., Halley, R.B., 1985. Burial Diagenesis: Out of Sight, Out of Mind!, vol. 36. SEPM Special Publication, pp. 309–334.
Scholle, P.A., Ulmer-Scholle, D., 2005. A Color Guide to the Petrography of Carbonate Rocks: Grains, Textures, Porosity, Diagenesis, vol. 77. AAPG Memoir, p. 486.
Scholle, P.A., Ulmer-Scholle, D.S., 2003. A Color Guide to the Petrography of Carbonate Rocks: Grains, Textures, Porosity, Diagenesis. American Association of Petroleum Geologists.
Semeniuk, V., 1992. The Pilbara Coast: a riverine coastal plain in a tropical arid setting, northwestern Australia. Sediment. Geol. 83, 235–256.
Semeniuk, V., 1996. Coastal forms and Quaternary processes along the arid Pilbara coast of northwestern Australia. Palaeogeogr. Palaeoclimatol. Palaeoecol. 123 (1), 49–84.
Semeniuk, V., 2008. Holocene sedimentation, stratigraphy, biostratigraphy, and history of the Canning Coast, North-Western Australia. J. Roy. Soc. West Aust. 91, 53–148.
Senders, M., Banimahd, M., Zhang, T., Lane, A., 2013. Piled foundations on the North West West Shelf. Aust. Geomech J. 48, 149–160.
Shinn, E.A., 1969. Submarine lithification of Holocene carbonate sediments in the Persian gulf. Sedimentology 12 (1–2), 109–144.
Short, A.D., 2006. Australian Beach System" Nature and Distribution.
Spagnoli, G., Scheller, P., 2016. Comparison between the Mixed-In-Place Technology and Driven Piles as Offshore Foundations. Abu Dhabi International Petroleum Exhibition & Conference.
Squire, P., Joannes-Boyau, R., Scheffers, A.M., Nothdurft, L.D., Hua, Q., Collins, L.B., Scheffers, S.R., Zhao, J.-x., 2013. A marine reservoir correction for the houtman-abrolhos Archipelago, east Indian ocean, western Australia. Radiocarbon 55 (1), 103–114.
Steneck, R.S.C.F.p.d, 1986. The ecology of coralline algal crusts: convergent patterns and adaptative strategies. Annu. Rev. Ecol. Systemat. 17, 273–303.
Stephen, J.G., Malcolm, W.W., Chung Leong, L., Belinda, K., John, T.B., Kazumi, A., Masayuki, T., 2009. Neogene history of the west pacific warm pool, kuroshio and Leeuwin currents. Paleoceanography 24 (1), PA1206.
Stow, D., 2005. Sedimentary Rocks in the Field: A Colour Guide.
Suppiah, R., 1992. The Australian summer monsoon: a review. Prog. Phys. Geogr. 16 (3), 283–318.
Teal, C.S., Mazzullo, S.J., Bischoff, W.D., 2000. Dolomitization of Holocene shallow-marine deposits mediated by sulfate reduction and methanogenesis in normal-salinity seawater, northern Belize. J. Sediment. Res. 70 (3), 649–663.
Vimpere, L., Del Piero, N., Le Cotonnec, A., Kindler, P., Castelltort, S., 2022. Depositional timing and palaeoclimate interpretation of the tamala limestone aeolianites in shark bay, western Australia. Aeolian Research 54, 100770.
Vora, K.H., Wagle, B.G., Veerayya, M., Almeida, F., Karisiddaiah, S.M., 1996. 1300 km long late Pleistocene-Holocene shelf edge barrier reef system along the western continental shelf of India: occurrence and significance. Mar. Geol. 134 (1), 145–162.
Vousdoukas, M.I., Velegrakis, A.F., Plomaritis, T.A., 2007. Beachrock occurrence, characteristics, formation mechanisms and impacts. Earth Sci. Rev. 85 (1), 23–46.
Warren, J., 2000. Dolomite: occurrence, evolution and economically important associations. Earth Sci. Rev. 52 (1), 1–81.
Webster, J., Dechnik, B., Sanborn, K., Yokoyama, Y., Braga, J., Renema, W., Humblet, M., Beamani, R., Nothdurft, L., Webb, G., Zhao, J.-x., Murphy, R., Gallagher, S., O'Leary, M., Paumard, V., 2022. Coral reef development and sea-level changes over the past 50,000 years: new evidence from the north-west shelf of Australia. IAS special publication: Coral Reefs and Sea-Level Change: Quaternary Records and Modelling 49, 215–273.
Webster, J.M., Davies, P.J., 2003. Coral variation in two deep drill cores: significance for the Pleistocene development of the Great Barrier Reef. Sediment. Geol. 159 (1), 61–80.
Weiss, A., Martindale, R.C., 2017. Crustose coralline algae increased framework and diversity on ancient coral reefs. PLoS One 12 (8), e0181637.
Wentworth, C.K.C.F.p.d.J.A, 1922. A scale of grade and class terms for clastic sediments. J. Geol. 30 (5), 377–392.
Whitney, B.B., Hengesh, J.V., Gillam, D., 2016. Styles of neotectonic fault reactivation within a formerly extended continental margin, North West Shelf, Australia. Tectonophysics 686, 1–18.
Wilson, B., 2013. Biogeography of the Australian North West Shelf Environmental Change and Life's Response. Elsevier Science, Saint Louis, p. 640.
Wiseman, C., O'Leary, M., Hacker, J., Stankiewicz, F., McCarthy, J., Beckett, E., Leach, J., Baggaley, P., Collins, C., Ulm, S., McDonald, J., Benjamin, J., 2021. A multi-scalar approach to marine survey and underwater archaeological site prospection in Murujuga, Western Australia. Quat. Int. 584, 152–170.
Yaalon, D.H., Laronne, J., 1971. Internal structures in eolianites and paleowinds, Mediterranean coast, Israel. J. Sediment. Res. 41 (4), 1059–1064.
Yokoyama, Y., De Deckker, P., Lambeck, K., Johnston, P., Fifield, L.K., 2001. Sea-level at the Last Glacial Maximum: evidence from northwestern Australia to constrain ice volumes for oxygen isotope stage 2. Palaeogeogr. Palaeoclimatol. Palaeoecol. 165 (3), 281–297.
Yokoyama, Y., Miyairi, Y., Aze, T., Yamane, M., Sawada, C., Ando, Y., de Natris, M., Hirabayashi, S., Ishiwa, T., Sato, N., Fukuyo, N., 2019. A single stage accelerator mass spectrometry at the atmosphere and ocean research Institute. The University of Tokyo. Nuclear Instruments and Methods in Physics Research Section B: Beam Interactions with Materials and Atoms 455, 311–316.
Yokoyama, Y., Purcell, A., Marshall, J.F., Lambeck, K., 2006. sea-level during the early deglaciation period in the Great barrier reef, Australia. Global Planet. Change 53 (1), 147–153.